



저작자표시-비영리-변경금지 2.0 대한민국

이용자는 아래의 조건을 따르는 경우에 한하여 자유롭게

- 이 저작물을 복제, 배포, 전송, 전시, 공연 및 방송할 수 있습니다.

다음과 같은 조건을 따라야 합니다:



저작자표시. 귀하는 원저작자를 표시하여야 합니다.



비영리. 귀하는 이 저작물을 영리 목적으로 이용할 수 없습니다.



변경금지. 귀하는 이 저작물을 개작, 변형 또는 가공할 수 없습니다.

- 귀하는, 이 저작물의 재이용이나 배포의 경우, 이 저작물에 적용된 이용허락조건을 명확하게 나타내어야 합니다.
- 저작권자로부터 별도의 허가를 받으면 이러한 조건들은 적용되지 않습니다.

저작권법에 따른 이용자의 권리는 위의 내용에 의하여 영향을 받지 않습니다.

이것은 [이용허락규약\(Legal Code\)](#)을 이해하기 쉽게 요약한 것입니다.

[Disclaimer](#)

공학박사 학위논문

**Integration of polymer and  
dye-sensitized solar cells for  
high voltage source**

고분자 및 염료 감응 태양 전지의 집적을  
통한 고전압 전원 활용에 관한 연구

2013 년 2 월

서울대학교 대학원  
공과대학 전기컴퓨터공학부

조 성 민

# Integration of polymer and dye-sensitized solar cells for high voltage source

지도교수 이 신 두

이 논문을 공학박사 학위논문으로 제출함

2013년 2월

서울대학교 대학원

공과대학 전기컴퓨터공학부

조 성 민

조성민의 박사 학위논문을 인준함

2012년 12월

위 원 장 \_\_\_\_\_ 박 남 규 (인)

부위원장 \_\_\_\_\_ 이 신 두 (인)

위 원 \_\_\_\_\_ 정 윤 찬 (인)

위 원 \_\_\_\_\_ 최 중 선 (인)

위 원 \_\_\_\_\_ 유 창 재 (인)

## **Abstract**

# **Integration of polymer and dye-sensitized solar cells for high voltage source**

Seong-Min Cho

School of Electrical Engineering and Computer Science

The Graduate School

Seoul National University

Organic solar cells (OSCs) such as polymer solar cells (PSCs) and dye-sensitized solar cells (DSCs) show great potential as a cost effective route to wide use of solar energy for electrical power generation. In the past decade, much effort has been focused on enhancing the power conversion efficiency (PCE) of OSCs. However, for practical electric power generation, the integration of OSCs is required as well as the efficiency enhancement of single OSC. In order to integrate OSCs, few unconventional patterning approaches have been proposed based on softlithographic or photolithographic methods. In spite of their many desirable properties including high pattern resolution, those methods have a limited applicability in the development of high-resolution OSCs with advanced performance due

to the pattern reliability and the restriction of patternable materials, and thus the development of a novel patterning method for organic/inorganic layers of OSCs is inevitably required

In this thesis, high-fidelity patterning techniques based on the use of a chemically compatible sacrificial layer, which is complementary transfer assisted lift-off (CTAL) technique, is studied in the viewpoint of the scientific research and practical applications to the integration of OSCs. The use of chemically compatible sacrificial layer of fluorine-polymer in combination with the softlithographic transfer-patterning provides the high-fidelity in patterning organic/inorganic layer without any detrimental effects on their electrical properties as well as the capability of high-resolution patterning down to a few micrometers.

First, I demonstrate integrated solid-state DSCs using a CTAL technique that can be used for patterning the nanocomposite  $\text{TiO}_2$  layer in a small area. By patterning electron transport layer of nanocomposite  $\text{TiO}_2$ , the individual cell can be integrated about a hundred micrometer scale. In addition, to resolve leakage and evaporation problem of liquid electrolyte, solid-state hole transport material of spiro-OMeTAD (2,20,7,70-tetrakis-(N,N-di-p-methoxyphenylamine)9,90-spirobifluorene) is used. This concept shows promise applicability of integrated DSCs to be a compact electric system.

Next, the PCE enhancement of PSCs in a bilayer configuration is demonstrated. Specifically, I describe the solvent-dependent morphology of a conjugated polymer, poly(3-hexylthiophene) (P3HT) interfaced with [6,6]-phenyl-C61-butyric acid methyl ester (PCBM) and the evolution of the

resulting inter-connected fibrillar structure (ICFS) in a diffusive bilayer heterojunction (DBHJ). It is found that the fibrillar structure of the P3HT is preferentially developed in a poor solvent and less soluble than an amorphous structure and the ICFS improves the PCE significantly. Among four different solvents of chlorobenzene, dichlorobenzene, chloroform, and *p*-xylene studied, *p*-xylene results in PCE  $\approx$  2.7% whereas chlorobenzene yields only 0.5%. This indicates clearly that the formation of the ICFS plays a critical role to induce high exciton generation/dissociation, to produce spatially uninterrupted pathways for the charge transport, and to enhance PCE of a single PSC device in the DBHJ configuration.

Finally, I develop a powerful platform of constructing polymer solar cells (PSCs) in a serial architecture within the framework of CTAL technique. The CTAL approach allows the feature resolution down to a few micrometers and provides high integration capability of different classes of functional materials including organic semiconductors, charge transporting materials, and metals. The sacrificial layer of hydrophobic fluorinate-polymer was patterned complementary to active regions, and lift-off of the sacrificial layer using a chemically inert solvent to leave only active patterns on a substrate. The reduced dark current by patterned hole transport layer of molybdenum oxide ( $\text{MoO}_x$ ) results in high open circuit voltage of integrated PSC array. A high voltage power source for electronic device was realized by interconnecting a PSC array to the liquid crystal display device. A monolithic integration of electronic device with self-power source will be the next step towards integrated organic devices.

In conclusion, through this thesis, a novel high-fidelity patterning technique, which is inevitably required for advanced solar cell systems, was shown with integrated PSCs and DSCs. Moreover, solvent-dependent fibrillar morphologies of the P3HT layer and the resultant PCBM-on-P3HT film play an important role in the PV characteristics were successfully demonstrated with sufficient experimental results. All this concept of highly integrated OSCs by CTAL patterning technique provides a versatile platform to devise a variety of compact electric and optoelectronic systems.

Keywords: polymer solar cells, dye-sensitized solar cells, integration, patterning, high voltage, diffusive bilayer, fibrillar morphology

Student Number: 2008-30886

# Contents

|  |          |
|--|----------|
| <b>Abstract</b>  | i        |
| <b>Contents</b>  | v        |
| <b>List of Tables</b>  | ix       |
| <b>List of Figures</b>   | x        |
| <b>Chapter 1 . Introduction</b> .....                          | <b>1</b> |
| <b>1.1 Solar Cells</b> .....                                   | 3        |
| <b>1.1.1 Principles of solar cells</b> .....                   | 3        |
| <b>1.1.2 Classification of solar cells</b> .....               | 7        |
| <b>1.2 Organic Solar Cells</b> .....                           | 9        |
| <b>1.2.1 Polymer solar cells</b> .....                         | 9        |
| <b>1.2.2 Dye-sensitized solar cells</b> .....                  | 13       |
| <b>1.3 Patterning Techniques for Organic Solar Cells</b> ..... | 16       |
| <b>1.3.1 Conventional methods</b> .....                        | 16       |
| <b>1.3.2 Softlithographic techniques</b> .....                 | 19       |
| <b>1.4 Outline of Thesis</b> .....                             | 22       |

## **Chapter 2 . Complementary Transfer Assisted Lift-Off**

|  |           |
|--|-----------|
| <b>Techniques .....</b>  | <b>24</b> |
| <b>2.1 Chemically Compatible Sacrificial Layer.....</b>                          | <b>26</b> |
| <b>2.2 Complementary Transfer Assisted Lift-Off .....</b>                        | <b>30</b> |
| <b>2.3.1 Transfer-patterning of sacrificial layer .....</b>                      | <b>30</b> |
| <b>2.3.2 Sacrificial layer assisted lift-off .....</b>                           | <b>32</b> |
| <b>2.3 Patterning of Charge Transport Layer in Organic Solar<br/>Cells .....</b> | <b>36</b> |
| <b>2.3.1 TiO<sub>2</sub> patterning .....</b>                                    | <b>36</b> |
| <b>2.3.2 MoO<sub>x</sub> patterning .....</b>                                    | <b>39</b> |

## **Chapter 3 . Integration of Solid-state Dye-sensitized Solar**

|  |           |
|--|-----------|
| <b>Cells.....</b>  | <b>41</b> |
| <b>3.1 Introduction.....</b>   | <b>41</b> |
| <b>3.2 Fabrication Process of Solid-State Dye-Sensitized Solar<br/>Cell Array.....</b> | <b>43</b> |
| <b>3.2.1 TiO<sub>2</sub> patterning technique .....</b>                                | <b>43</b> |
| <b>3.2.2 Fabrication process of solar cell array .....</b>                             | <b>45</b> |
| <b>3.3 Patterned TiO<sub>2</sub> Film in Micrometer Scale.....</b>                     | <b>48</b> |

|                  |   |           |
|------------------|---|-----------|
| 3.4              | Solar Cell Characteristics.....   | 50        |
| 3.5              | Summary.....  | 52        |
| <br>             |   |           |
| <b>Chapter 4</b> | <b>Polymer Solar Cells .....</b>  | <b>53</b> |
| <b>4.1</b>       | <b>Efficiency Enhancement of Polymer Solar Cells in a Bialyer Configuration.....</b>          | <b>53</b> |
| 4.1.1            | Introduction .....  | 53        |
| 4.1.2            | Fabrication process of polymer solar cells with inter-connected fibrillar structures .....    | 55        |
| 4.1.3            | Solvent-dependent fibrillar morphologies of polymer .....                                     | 58        |
| 4.1.4            | Photovoltaic characteristics.....   | 66        |
| 4.1.5            | Summary.....  | 69        |
| <b>4.2</b>       | <b>Integrated Polymer Solar Cells with MoO<sub>x</sub> Layer for High-voltage Source.....</b> | <b>71</b> |
| 4.2.1            | Introduction .....  | 71        |
| 4.2.2            | Modeling the integrated polymer solar cells with patterned HTL.....                           | 74        |
| 4.2.3            | Fabrication process of integrated polymer solar cell .....                                    | 76        |
| 4.2.4            | Solar cell characteristics.....   | 78        |
| 4.2.5            | Applicability for power source of electronic devices.....                                     | 84        |

|   |            |
|---|------------|
| 4.2.6 Summary.....                          | 87         |
| <b>Chapter 5 . Concluding Remarks .....</b> | <b>88</b>  |
| <b>Bibliography .....</b>                   | <b>91</b>  |
| <b>Publication .....</b>                    | <b>100</b> |

## List of Tables

|  |    |
|--|----|
| Table 2.1 The physical properties of HFE-7100. ....  | 28 |
| Table 2.2 The physical properties of EGC-1700 .....  | 28 |
| Table 3.1 The values of $J_{sc}$ , $V_{oc}$ , FF, and PCE in single and 20 ss-DSC array devices .....  | 51 |
| Table 4.1 The values of $J_{sc}$ , $V_{oc}$ , FF, and $\eta_p$ in several DBHJ PV devices with the P3HT layers produced using four different solvents..... | 69 |
| Table 4.2 The values of $J_{sc}$ , $V_{oc}$ , FF, and PCE in single and 20 PSC array devices with patterned $MoO_x$ layer and whole $MoO_x$ layer. ....    | 84 |

## List of Figures

|   |    |
|---|----|
| Figure 1.1 Power cost targets for solar power, oil-fired thermal power and nuclear power generation. (The graph is taken from ref. [5].) .....  | 2  |
| Figure 1.2 Schematic diagrams of a conventional p-n junction solar cell [7]..   | 3  |
| Figure 1.3 (a) Equivalent circuit of solar cell. (b) Graph of current versus voltages for solar cell .....  | 4  |
| Figure 1.4 Classification of solar cells .....  | 7  |
| Figure 1.5 Progression of the best efficiencies for current solar cell technologies.....  | 8  |
| Figure 1.6 Steps in the photocurrent generation process. The horizontal lines to the right and left of each illustration correspond to the Fermi energies ( $E_F$ ) of the cathode and anode contacts, respectively. The boxes correspond to the acceptor (left) and donor (right) energy gaps, respectively. Here, LUMO and HOMO are the lowest unoccupied molecular orbital and the highest occupied molecular orbital of the organic film, respectively..... | 11 |
| Figure 1.7 (a) Schematic diagram of dye-sensitized solar cell. (b) Energy level diagram with the fundamental process of dye-sensitized solar cell .....   | 14 |
| Figure 2.1 The chemical structure of HFE-7100 (mixture of two isomers)...   | 26 |
| Figure 2.2 The chemical structure of EGC-1700. (The schematic is taken from ref. [41]) .....  | 27 |

|   |    |
|---|----|
| Figure 2.3 Schematic diagram of the process of transfer-printing based on the work of adhesion .....  | 31 |
| Figure 2.4 Schematic diagram of the process of complementary transfer assisted lift-off technique .....   | 33 |
| Figure 2.5 The pattern examples of sacrificial layer films with various pattern features fabricated using transfer-printing.....  | 35 |
| Figure 2.6 (a) Optical microscopic and (b), (c) FE-SEM images of patterned TiO <sub>2</sub> layer. The inset shows the FE-SEM image of the TiO <sub>2</sub> nanoparticles in high resolution .....  | 37 |
| Figure 2.6 High resolution FE-SEM images of TiO <sub>2</sub> layer after cutting.....   | 38 |
| Figure 2.7 Solid state <sup>19</sup> F-NMR spectrums of (a) empty rotor and (b) TiO <sub>2</sub> nanoparticles after CTAL patterning which using fluorous-solvent. ....   | 39 |
| Figure 2.8 Optical microscopic images of MoO <sub>x</sub> patterns showing (a) circles of 50 μm diameter and (b) squares of 25 μm in each side. ....  | 40 |
| Figure 3.1 Schematic diagram of the solid-state DSC array. Solid-state DSC comprised of transparent FTO on glass, nanoparticle photoanode of TiO <sub>2</sub> covered in a monolayer of sensitizing dye, hole transport material for solid-state electrolyte, and gold back electrode. .... | 42 |
| Figure 3.2 Schematic diagram of the solid-state DSC array. Solid-state DSC comprised of transparent FTO on glass, nanoparticle photoanode of TiO <sub>2</sub> covered in a monolayer of sensitizing dye, hole transport material for solid-state electrolyte, and gold back electrode.....  | 44 |

Figure 3.3 Schematic diagram of the solid-state DSC array. Solid-state DSC comprised of transparent FTO on glass, nanoparticle photoanode of TiO<sub>2</sub> covered in a monolayer of sensitizing dye, hole transport material for solid-state electrolyte, and gold counter electrode.. 46

Figure 3.4 Chemical structures of (a) Z907 dye [67] and (b) spiro-OMeTAD [68] ..... 47

Figure 3.5 (a) Optical microscopic and (b)~(d) FE-SEM images of patterned TiO<sub>2</sub> layer. (c) The cross-sectional image of TiO<sub>2</sub> film. (d) The enlarged image of TiO<sub>2</sub> film composed of the TiO<sub>2</sub> nanoparticles. .... 48

Figure 3.6 (a) Dye adsorbed nanocrystalline TiO<sub>2</sub> film of 20 array. (b) Fabricated ss-DSC array after spin-coating of spiro-OMeTAD and gold deposition ..... 49

Figure 3.7 The current-voltage curves of (a) single and (b) 20 ss-DSC array under the AM 1.5 100mW/cm<sup>2</sup> illumination. .... 50

Figure 4.1 Schematic diagram showing the cross-section of (a) an organic PV device with the DBHJ active layer. (b) Possible types of interfacial regions; inter-diffusive structures (IDS) and inter-connected fibrillar structures (ICFS) ..... 56

Figure 4.2 The AFM images and the corresponding morphological profiles of the P3HT layers prepared from four different solvents: (a) the PX, (b) the CB, (c) the DCB, and (d) the CF. The AFM images were obtained with scanning an area of 1.5 μm x 1.5 μm.

|            |   |    |
|------------|---|----|
|            | Morphological profiles were obtained along the black lines in the AFM images. ....  | 59 |
| Figure 4.3 | (a) The out-of-plane GIXRD diffractograms for the incident angle of 0.5° and (b) the UV-visible absorption spectra of the P3HT layers prepared with different solvents.....   | 61 |
| Figure 4.4 | The AFM images and the corresponding morphological profiles of the P3HT layers prepared from (a) the PX and (b) the DCB after the solvent annealing with the PX: The left column shows the amplitude images and the right column shows the phase images. Morphological profiles were obtained along the black lines in the amplitude images. (c) The UV-visible absorption spectra of (a) and (b) ..... | 63 |
| Figure 4.5 | The AFM images of the PCBM-on-P3HT films prepared from (a) the PX and (b) the DCB where the PCBM solution in the PX was spin-coated: The left and right columns are the amplitude and phase images, respectively. (c) The UV-visible absorption spectra of (a) and (b).....   | 65 |
| Figure 4.6 | Current-voltage characteristics of several DBHJ PV devices with the PCBM-on- P3HT films: the CF-P3HT (open circles), the CB-P3HT (open squares), the DCB-P3HT (open triangles), the PX-P3HT (open diamonds), and the PX-P3HT with the PA treatment (closed diamonds). ....  | 67 |
| Figure 4.7 | The schematic illustration of (a) a PSC with hole transport layer (HTL) and (b) a PSC array structure with patterned HTL .....  | 73 |

|             |  |    |
|-------------|--|----|
| Figure 4.8  | The schematic illustration of (a) a PSC with hole transport layer (HTL) and (b) a PSC array structure with the patterned HTL....   | 74 |
| Figure 4.9  | (a) The fabrication process for SLAP and the corresponding microscopic image of top-view of (b) the patterned SL and (c) the patterned MoO <sub>x</sub> . The schematic diagram of the top-view of the fabricated PSC array with interconnected area.....  | 77 |
| Figure 4.10 | Current-voltage characteristics of single PSC devices with the hole transport layer of PEDOT:PSS and MoO <sub>x</sub> .....  | 79 |
| Figure 4.11 | Current-voltage curves of 20 PSC array with patterned (red) and whole (black) MoO <sub>x</sub> layer (a) under the AM 1.5 100mW/cm <sup>2</sup> illumination and (b) in the dark.....  | 81 |
| Figure 4.12 | Current-voltage curves of 50 PSC array with patterned (red) and whole (black) MoO <sub>x</sub> layer (a) under the AM 1.5 100mW/cm <sup>2</sup> illumination and (b) in the dark.....  | 82 |
| Figure 4.13 | The LCD device (a) operated by PSC array and (b) the normalized electro-optic transmittance as a function of the applied voltage. ....   | 85 |
| Figure 4.14 | Drain-source current-voltage characteristics of the OFET with gate bias voltage generated by the 50 PSC array under simulated solar irradiation and light off. The inset shows the electronic circuitry of the interconnected PSC array and the OFET. .... | 86 |

# Chapter 1. Introduction

Energy plays a fundamental role in shaping the human condition. People's need for energy is essential for survival, so it is not surprising that energy production and consumption are some of the most important activities of human life. According to the investigations of the U.S energy information administration, the world energy demand in 2010 has reached 15 TW [1]. The energy demand is grow an annual rate of 2.4%, and will reach 30 TW by 2040 [2, 3]. However, about 80% of the present energy comes from fossil fuels and the limiting supply of fossil fuels will force us to substitute the current fossil fuels by renewable energy sources. In addition, fossil fuels occurs the environment problems due to the by-products of carbon dioxide (CO<sub>2</sub>) gas. Within 200 years of industrialization, the level of CO<sub>2</sub> in the atmosphere has already increased from 280 ppm to 380 ppm. And, we must keep atmospheric CO<sub>2</sub> below 450 ppm which is believed will keep global warming down to 2 °C increase in average global temperature [3]. Therefore, renewable sources such as wind, hydroelectric, geothermal, bio mass and solar photovoltaic are researched and utilized as a substitute for fossil fuels. Among the various renewable energy technologies, solar photovoltaics that directly convert energy of sunlight into electricity have attracted a lot of interest both from scientific research and industrial production due to their abundance and cleanliness [4]. In order to replace the fossil fuels, the power cost of solar cells

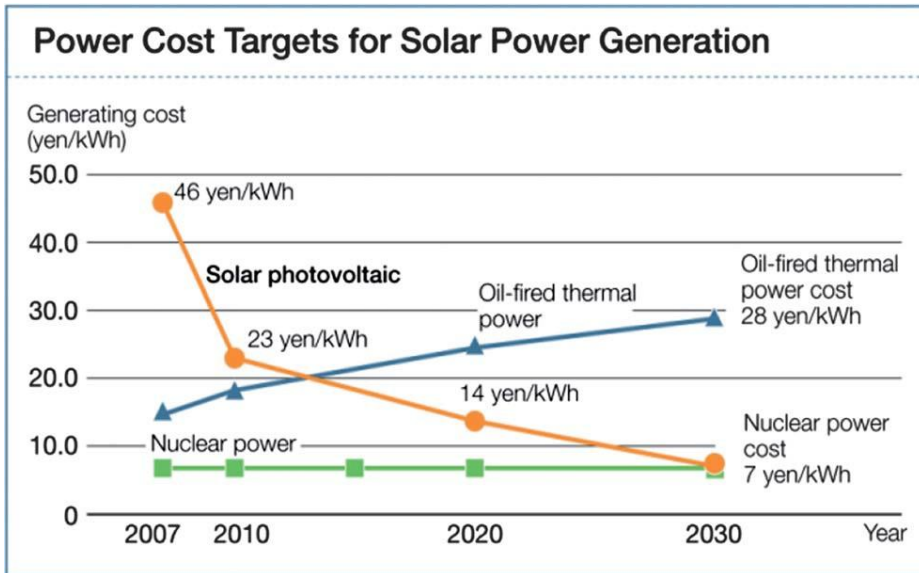


**Figure 1.1** Power cost targets for solar power, oil-fired thermal power and nuclear power generation. (The graph is taken from ref. [5].)

has to be decreased because of the higher cost comparing with traditional power sources, as shown in Fig.1.1.

Therefore, it is necessary and challenging to make significant technology improvement in both device performance and the manufacturing process so that solar cells could be economically competitive for electrical power generation.

In this thesis, organic solar cells based on polymer and dye-sensitized are presented, in the view point of efficiency enhancement of single device and integration technique for improvement of array device fabrication. First of all, in this chapter, the operating principles and required patterning process for organic solar cells are briefly introduced.

## 1.1 Solar Cells

### 1.1.1 Principles of solar cells

A solar cell device consists of a light absorbing material which is connected to an external circuit in an asymmetric manner, as shown in Fig. 1.2. Light is made up of packets of energy, called photons, whose energy depends only upon the frequency, or color, of the light [6]. Charge carriers are generated in the light absorbing materials and are driven towards one or other of the contacts by the built-in spatial asymmetry. This light driven charge separation establishes a photovoltage at open circuit, and generates a photocurrent at short circuit. When a load is connected to the external circuit, the cell produces both current and voltage and can do electrical work.

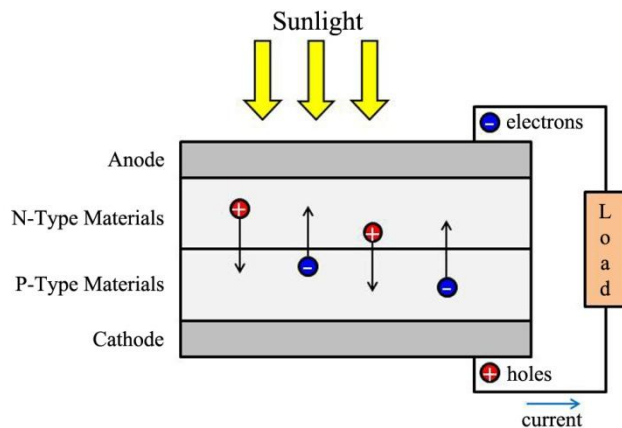


**Figure 1.2** Schematic diagrams of a conventional p-n junction solar cell [7].

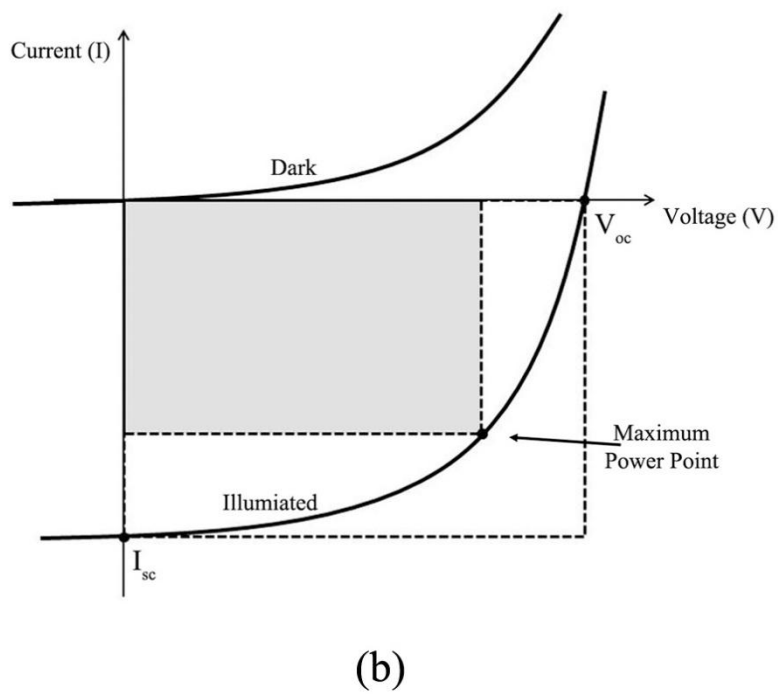
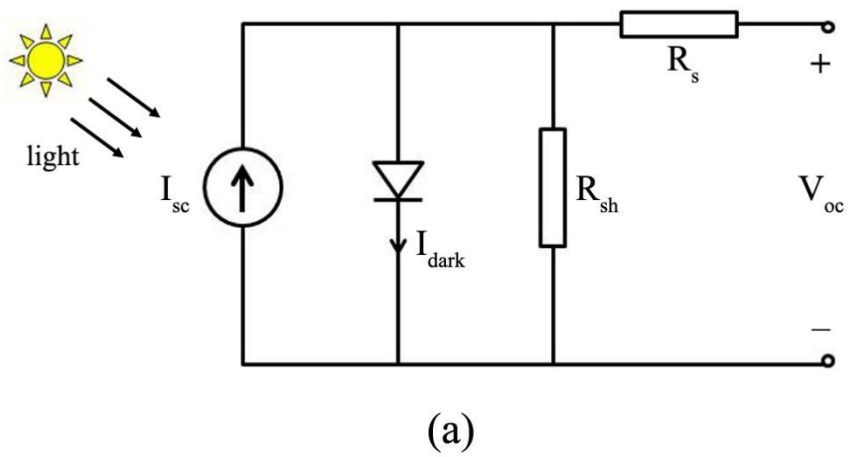


**Figure 1.3** (a) Equivalent circuit of solar cell. (b) Graph of current versus voltages for solar cell.

Figures 1.3(a) and (b) show equivalent circuit and current (I) versus voltage (V) curves of solar cell. When the solar cell is exposed to the light, the current flows through an illuminated solar cell. If there is no external resistance, the maximum current can be produced. This is called short-circuit current ( $I_{sc}$ ). In real cells, power is dissipated through the resistance of the contacts and through leakage currents around the sides of devices. These effects are equivalent electrically to two parasitic resistances in series ( $R_s$ ) and in parallel ( $R_{sh}$ ) with the cell, as shown in Fig. 1.3(a) [6]. The open circuit voltage ( $V_{oc}$ ) has been defined as the maximum possible voltage across a solar cell when the no current is flowing.

The sun light attenuated by the earth atmosphere. This is denoted as Air Mass( $x$ ) (A.M.), where  $x$  is the inverse of the cosine of zenith angle of the sun. A typical value for solar cell measurements is A.M. 1.5, which means that the sun is at an angle of about  $48^\circ$  [7]. In the dark, the I-V curve passes through the origin with no potential and no current flows, as shown in Fig. 1.3(b). The dark current is generated by a potential difference between the terminals of the cell. This potential difference generates a dark current which acts in the opposite direction to the photocurrent, and the net current is reduced from its short circuit current.

The power (P) is the product of current and voltage ( $P = I \cdot V$ ) and as illustrated in the Fig. 1.3(b), the area of the rectangle formed between a point on the I-V curve and the axes. The maximum power point is the point on the I-V curve where the area of the resulting rectangle is largest. The fill factor (FF) is defined as the ratio of a solar cell's actual maximum power output to

its theoretical power output if both current and voltage were at their maxima,  $I_{sc}$  and  $V_{oc}$ , respectively. The FF is defined as the ratio

$$FF = \frac{I_m V_m}{I_{sc} V_{oc}} . \quad (1.1)$$

The power conversion efficiency (PCE or  $\eta_e$ ) is the ratio of power output to power input. In other words, PCE measures the amount of power produced by a solar cell relative to the power available in the incident solar radiation ( $P_{in}$ ). The  $P_{in}$  is sum over all wavelengths and is generally fixed at  $100 \text{ mW/cm}^2$  when solar simulators are used. The formula for PCE, in terms of quantities defined above, is

$$\eta_e = \frac{I_{sc} V_{oc} FF}{P_{in}} . \quad (1.2)$$

### 1.1.2 Classification of solar cells

The solar cells have various types according to their materials, as shown in Fig. 1.4 [6, 8]. Among them, the conventional crystalline silicon (Si) solar cells, the first generation of solar cells, have elevated solar cell industry into a leading system of renewable energy and show highest efficiency, as shown in Fig 1.5 [9]. In spite of a substantial drop in the cost over the past 50 years, solar cells based on Si materials are currently not economically feasible because of the higher cost comparing with traditional power sources. The second generation cells based on thin films such as CdTe,  $\text{CuIn}_{1-x}\text{Ga}_x\text{Se}_2$  and

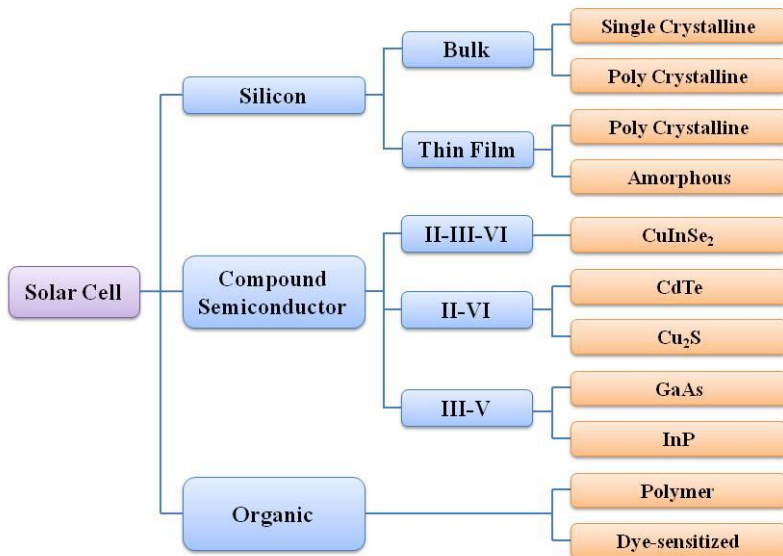


**Figure 1.4** Classification of solar cells.

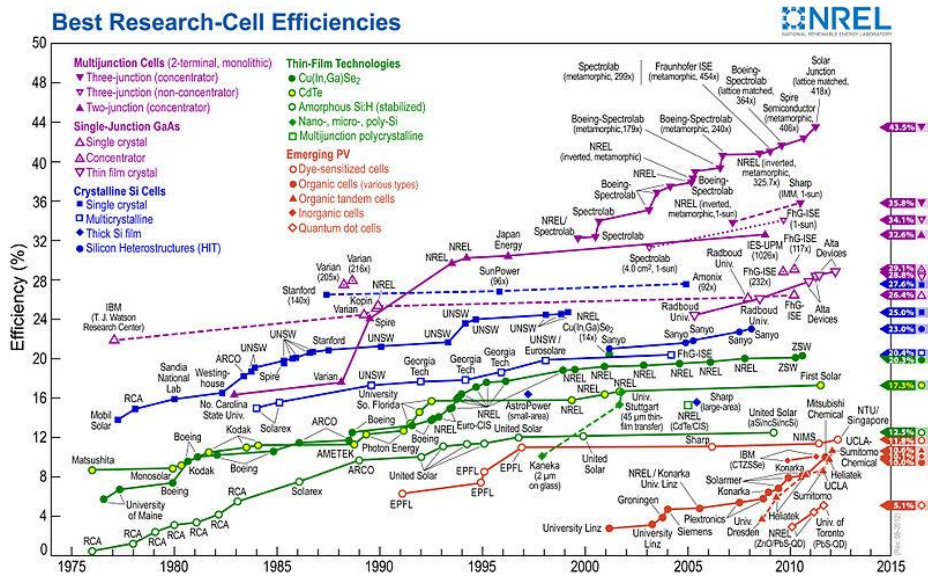


**Figure 1.5** Progression of the best efficiencies for current solar cell technologies [9].

hydrogenated amorphous Si have lower efficiency, but the low cost per power is lower than that of the first generation cells [10]. For the coming third generation or emerging photovoltaics (PVs), such as polymer, dye-sensitized, and quantum dot cells are considered as one of the most promising technologies to achieve the goal of both high efficiency and low cost [11]. In particular, organic solar cell (OSC) such as polymer solar cell (PSC) and dye-sensitized solar cell (DSC) are very promising and reported extensively due to their significantly lower manufacturing and installation costs, materials versatility, and mechanical flexibility [12-14].

## 1.2 Organic Solar Cells

### 1.2.1 Polymer solar cells

The first OSC was demonstrated by C. W. Tang [15]. The first OSC was comprised of copper phthalocyanine (CuPc) and perylene bilayer between ITO anode and Ag cathode. The device showed a maximum PCE of 1%. Then, A. J. Heeger *et al.* reported the OSC structure which consists of the conducting polymer and fullerene (C<sub>60</sub>) [16]. They reported the photo-induced charge transfer from the excited state of a conducting polymer onto C<sub>60</sub>. After that, great progress based on conducting polymer has been achieved. As shown in Fig. 1.5, the PCE of PSCs has been increased rapidly, and reached 10% [8].

#### *Operation principles of PSCs*

Photoexcitations in PSCs are inherently different from those in conventional inorganic solar cells. In organic semiconductors, light absorption almost result in the production of excitons, which is tightly bound electron-hole pairs than free electrons because of two reasons [17]. First, the dielectric constant of the organic phase is usually low compared to inorganic semiconductors. The attractive coulomb potential well around the incipient electron-hole pair extends over a greater volume than it does in inorganic semiconductors. Second, the noncovalent electronic interactions between

organic molecules are weak compared to the strong interatomic electronic interactions of covalently bonded inorganic semiconductor materials like silicon. Thus, the electron's wave function is spatially restricted, allowing it to be localized in the potential well of its conjugate hole. Therefore, a tightly bound electron-hole pair (Frenkel exciton or mobile excited state) is produced by light absorption in organic semiconductors as shown in Fig. 1.6 (a) [18].

The exciton is a mobile, electrically neutral species which is unaffected by electric fields. In order to generate free carriers, the excitons must be dissociated. This can happen in the presence of high electric fields, at a defect site in the material or at the interface between two materials with a sufficient mismatch in their energetic levels. The fundamentally important process is the interfacial dissociation of excitons at a hetero-interface into a free electron in one material (electron acceptor) and a free hole on the other side of the interface (electron donor). Therefore, excitons must diffuse to the hetero-interface in order to dissociate, as shown in Fig. 1.6 (b).

Charge carrier generation is simultaneous with the charge separation across the hetero-interface as shown in Fig. 1.6(c). This gives rise to a large chemical potential energy gradient  $\nabla\mu$  which by itself is a powerful PV driving force [18].

Figure 1.6(d) shows charge collection in PSCs. In general, it has been found that the charge collection and charge transfer efficiencies at organic donor,acceptor interfaces commonly used in thin-film molecular organic semiconductor PV cells approach 100%.

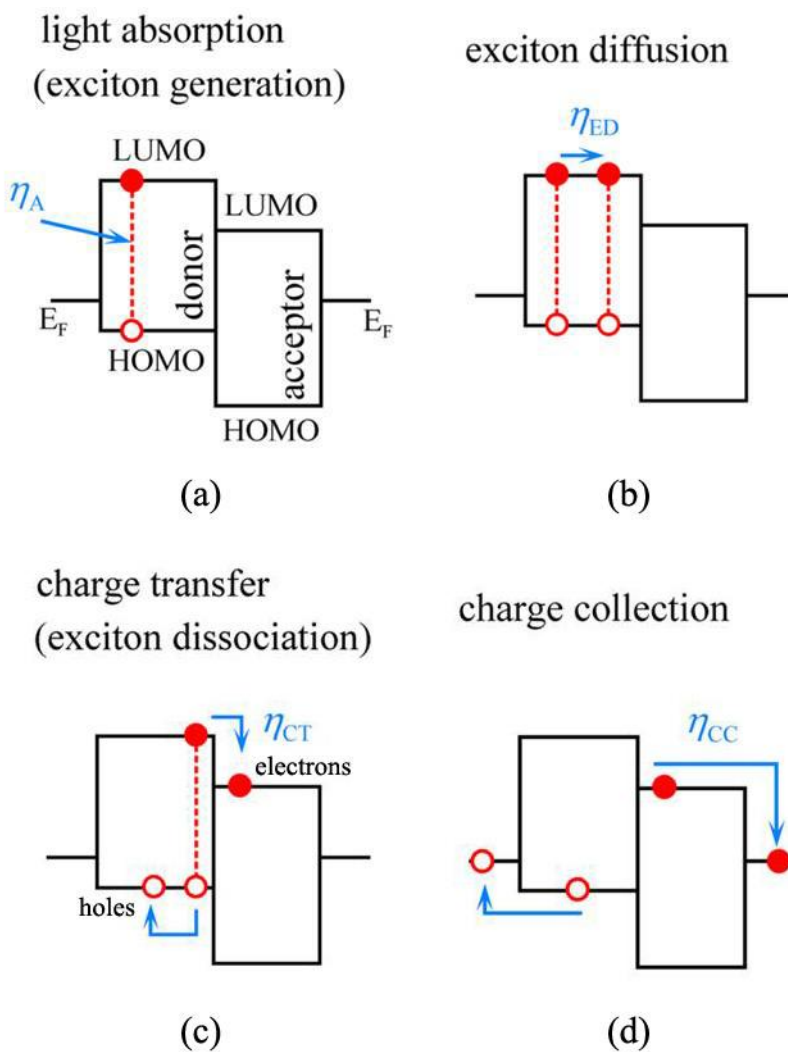


**Figure 1.6** Steps in the photocurrent generation process. The horizontal lines to the right and left of each illustration correspond to the Fermi energies ( $E_F$ ) of the cathode and anode contacts, respectively. The boxes correspond to the acceptor (left) and donor (right) energy gaps, respectively. Here, LUMO and HOMO are the lowest unoccupied molecular orbital and the highest occupied molecular orbital of the organic film, respectively.

The internal quantum efficiency of  $\eta_{IQE}$  is the product of four efficiencies [19]

$$\eta_{IQE} = \eta_A \eta_{ED} \eta_{CT} \eta_{CC}, \quad (1.3)$$

where  $\eta_A$  is the absorption efficiency of light within the active region of the solar cell,  $\eta_{ED}$  is the exciton diffusion efficiency to a dissociation site,  $\eta_{CT}$  is the charge transfer efficiency which is the efficiency for dissociation of an exciton into a free electron and hole pair at that site, and  $\eta_{CC}$  is the charge collection efficiency. Taking into consideration the optical losses that occur on coupling light in the device active region, the external quantum efficiency of  $\eta_{EQE}$  is given by

$$\eta_{EQE} = (1 - R) \eta_{IQE}, \quad (1.4)$$

where  $R$  is the reflectivity of the substrate-air interface.

PSCs have several limitations that are shown in Eq. (1.3) and Eq. (1.4). Among them, the exciton diffusion bottleneck significantly limits their PCE. Note that, there is an inherent tradeoff between the absorption and the exciton diffusion efficiencies. That is, the exciton diffusion length  $L_D$ , is typically much less than the optical absorption length  $1/\alpha$ . For an absorbing organic layer of thickness  $d$ ,

$$\eta_A = 1 - e^{-\alpha d}, \quad (1.5)$$

whereas, assuming that the arrival of excitons at a dissociation site is independent of electric fields or other extrinsic conditions, the diffusion efficiency is given by

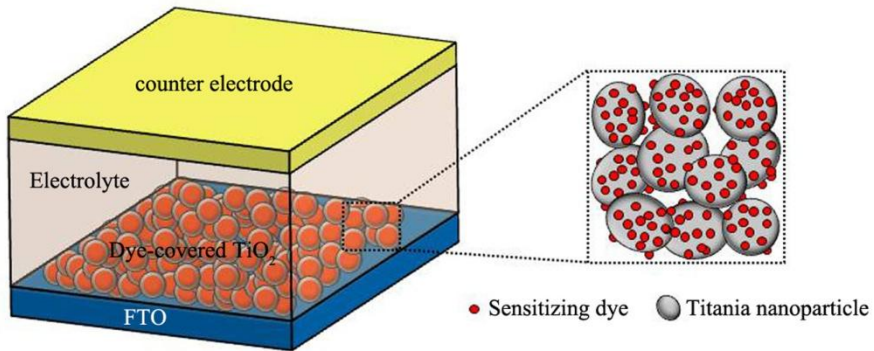
$$\eta_{ED} = e^{-d/L_D}. \quad (1.6)$$

### 1.2.2 Dye-sensitized solar cells

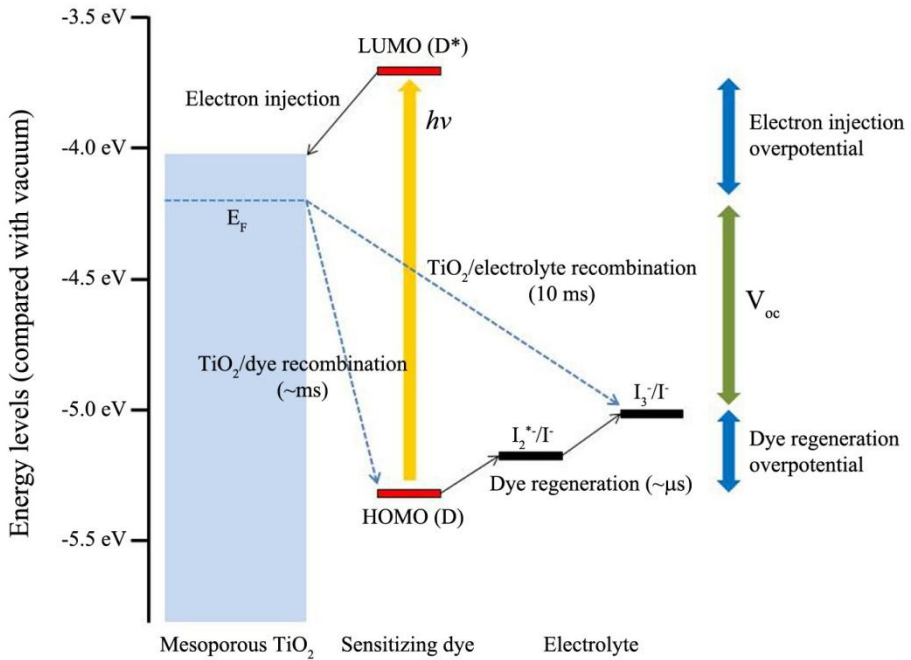
DSCs have attracted considerable attention in recent years as they offer the possibility of low cost conversion of photovoltaic energy. The first DSC was demonstrated in 1991 by O'Regan and Gratzel that a film of titania ( $\text{TiO}_2$ ) nanoparticles deposited would act as a mesoporous n-type photoanode and thereby increase the available surface area for dye attachment [20]. This approach dramatically improved light absorption and brought PCE into a range that allowed the DSCs to be viewed as a bright future of next generation solar cells. The record power-conversion efficiency rapidly climbed to 10% in the late 1990s and then slowly settled to 11.5% with the organometallic complexes based on ruthenium dye and iodide/triiodide ( $\text{I}/\text{I}_3$ ) system [8].

#### *Operation principles of DSCs*

Figure 1.7 shows a schematic and energy level diagram of a typical DSC. Conventional DSCs contain five components. These are a photoanode, a mesoporous semiconductor metal oxide film, a sensitizer (dye), an electron/donor transporter, and a counter electrode, as shown in Fig. 1.7(a) [21]. In DSCs, the incoming light is absorbed by the dye, which is anchored to the surface of semiconducting nanostructured titanium dioxide ( $\text{TiO}_2$ ). The porous  $\text{TiO}_2$  layer is interpenetrated by a hole-transport material (HTM), which may be a redox electrolyte in solution or a solid-state or a quasi-solid-state (gel) material [22]. Excited dye leads to the injection of electrons from t-



(a)



(b)

**Figure 1.7** (a) Schematic diagram of dye-sensitized solar cell. (b) Energy level diagram with the fundamental process of dye-sensitized solar cell.

he dye to the conduction band of the  $\text{TiO}_2$ . The ground state of the dye is regenerated through reduction by the HTM to give the required charge separation. Charges migrate and are collected at a transparent electrode (electrons) and Pt electrode (holes). In conventional DSCs, the  $\text{I}/\text{I}_3^-$  in solution systems show high efficiencies because of the slow recombination kinetics between electrons in the titania with the oxidized dye and triiodide in the electrolyte, which result in long-lived electron lifetime (between 1ms and 1 s), as shown in Fig. 1.7(b) [23, 24]. However, the  $\text{I}/\text{I}_3^-$  system is corrosive and dissolves many of the commonly used sealants and metal interconnects such as silver, copper, aluminum, and gold, especially at elevated temperature. In addition to poor long-term stability, manufacturing complexity is another problem in liquid electrolyte system [25]. In particular, sealing walls for each cell makes complicated to integrate DSC arrays. Therefore, the solid-state DSCs are attracted increasing attention in recent years, due to their capability to solve the leakage and sealing problems that exist in liquid type DSCs [26–28]. However, the patterning technique for  $\text{TiO}_2$  nanoparticles, which is inevitably required in array fabrication, has not been developed so far.

## **1.3 Patterning Techniques for Organic Solar Cells**

For organic electronics including OSCs, simple and reliable patterning techniques have great importance for the construction of basic components and the fabrication of device array in a small area. It is critical to pattern organic/inorganic layers without causing the degradation of the characteristics of organic electronics in the subsequent device fabrication.

### **1.3.1 Conventional methods**

#### ***Shadow mask patterning for vacuum thermal evaporation***

Vacuum thermal evaporation is common methods for depositing materials onto a substrate. A thermal evaporator uses an electric resistance heater to melt the material and raise its vapor pressure to a useful range. This is done in a high vacuum, both to allow the vapor to reach the substrate without reacting with or scattering against other gas-phase atoms in the chamber, and reduce the incorporation of impurities from the residual gas in the vacuum chamber. Vacuum thermal evaporation is widely used in the processing of inorganic semiconductor devices due to the precision with which layer thickness can be controlled within 0.5 nm, and the relative simplicity of the process. One major advantage of thermal deposition is its ability to grow an unlimited number of layers, each optimized for a different function, to complete the device structure. This flexibility in device design is an inherent feature of dry

processing that is, the several material layers that are deposited to form a device structure do not physically interact because there is no solvent that might transport material and chemically attack the pre-deposited material. In thermal deposition, various patterns can be easily produced by adding a shadow mask, which is usually a thin metal with holes of desired patterns, between a source material and a substrate in a vacuum chamber. However, the pattern size is limited by 40  $\mu\text{m}$ , due to the size limitation of metal mask [29]. And the blurs and errors can be generated, as the size of substrate increases or the features become smaller, by the sagging of thin metal mask because of the gravitational force, resulting in the limitation of pattern resolution over large-area. In addition, a lot of material lost and the substrate heating during the process are another disadvantages of this method.

### ***Ink-jet printing***

Inkjet printing is a commonly used technique for controlled deposition of solutions of functional materials in specific locations on a substrate and can provide easy and fast deposition of polymer films over large area [30]. In addition, inkjet printing is promising because the polymer devices can be fabricated very easily due to the compatibility with various substrates and need of no additional patterning. Inkjet printing has been used in the field of polymer solar cell, polymer light emitting diodes, and thin film transistors [30-33]. However, it is still difficult to produce precise patterns through inkjet printing since the pattern dimension is usually determined by the range where the polymer ink spread out. Therefore, some kinds of preprocessing is

additionally required such as a fabrication of well structures to physically block the spread of polymer ink. Such structures might limit the freedom of designing device structures, and thus various surface treatments using oxygen plasma or UV ozone are recently attracted much attention to locally control the surface wettability.

### ***Photolithographic technique***

Photolithographic techniques have been widely used in the inorganic semiconductor industry, which have the capability of high-resolution and high-throughput as well as the availability of well-established equipments and expertise. Patterning of thin films based on the photolithographic process can be generally divided into two different methods, one of which is ‘additive’ and the other is ‘subtractive’. In the ‘additive’ method, the target film is deposited onto the preformed photoresist patterns and subsequently lifted-off by removing the photoresist simultaneously with the residual thin films on it, leaving only the desired film patterns on a substrate. On the contrary, the etching process is used in the ‘subtractive’ method. The photoresist is patterned on a predeposited thin film to be used as a etch mask. The following etching process to erase the thin film exposed to the solvent or using dry-etching completes the pattern generation on a substrate. Such two types of photolithographic patterning processes commonly have not been used in fabrication of organic electronic devices mainly due to the chemical incompatibility. Recently, an advanced photolithographic method, based on the use of an orthogonal solvent dissolving a new type of a photoresist [34,

35], is promising for fabricating organic electronic devices. However, this photolithography still involves the patterning complexity and may experience the deterioration of underlying organic layers in multilayer architecture by the exposure of strong ultraviolet (UV) light.

### **1.3.2 Soft-lithographic techniques**

Soft-lithography is the most widely used unconventional patterning technique for the fabrication of organic electronic devices. Recently, a number of unconventional patterning methods based on soft-lithographic techniques studied for the fabrication of PSCs [36], DSCs [37], organic thin-film transistors (OTFTs) [38], and organic light-emitting diodes (OLEDs) [39]. These include embossing, microcontact printing ( $\mu$ CP), imprint lithography, soft contact lamination, and transfer printing [40]. The characteristics of several representative unconventional patterning approaches are briefly described.

#### ***Embossing***

A typical embossing process begins with casting of a solution or liquid precursor of a uniform thin film of organic materials on a solid substrate. The casting procedures such as rod casting, spin casting, and drop casting, define the thickness and thickness uniformity of the film. Embossing can create relief on the surfaces of organic films composed of most materials, ranging from inert polymers for waveguide claddings, to active polymers and small organic

molecules for functional devices, to liquid precursors, if their viscosities are sufficiently low.

### ***Microcontact printing ( $\mu$ CP)***

The  $\mu$ CP is one of the soft lithography that uses the relief pattern on a master PDMS stamp to form patterns of self-assembled monolayers of ink on the surface of a substrate through conformal contact. The  $\mu$ CP method can be used in several different ways. The pattern generated by the printing can function as an etch mask or it can become a patterned active area or it can define the electrodes. It can also be used as wetting patterns in which materials are deposited on the printed regions and not on the bare regions, in contrast to the general soft-lithographic methods.

### ***Imprint lithography***

Imprint lithography combines embossing of films with a subsequent etching step that removes the thin regions to produce these types of isolated features. It is noted that embossing process, unlike imprint lithography, produces relief structures in films or on substrate surfaces. This type of approach has the potential for large-area, low-cost fabrication on both flat and nonflat substrates with low pressure and at room temperature.

### ***Soft contact lamination***

Often in organic optoelectronics, two or more device components must be prepared using incompatible processes. Fabrication of a device in two

separate parts that can be joined together offers process flexibility. This strategy is the principle of lamination. Lamination is similar to stamp-based printing approaches in the sense that two bodies are joined for the fabrication and patterning of the materials, but in the case of lamination, the devices are formed by the union of the two bodies and no materials are transferred.

### ***Transfer printing***

Transfer printing techniques that use stamps have been successfully applied to many areas of organic electronics and optoelectronics. Their ability to pattern large areas in a single process step and their high resolution represent key features of these approaches. Generally, a stamp supplies a chemical or material to a substrate by physical contact. In contrast to  $\mu$ CP, transferred material acts as either a functional layer of a device, a resist for etching underlying materials, or a catalyst for directing the deposition or growth of other materials. In particular, transfer printing can be used for multiple layers. Resolution limited by the resolution of the stamps themselves or the materials characteristics of the inks resulting in high resolution. In many instances, stamping methods reduce the number of process steps by minimizing the use of sacrificial layers or even eliminating them by employing purely additive approaches. The requirements for transfer printing are similar to those for  $\mu$ CP: (i) a stamp that can support a functional ink and can be contacted to a target substrate and (ii) some mechanism for the transfer of this ink from the stamp to the substrate [40].

## 1.4 Outline of Thesis

This thesis is composed of five chapters including **Introductions** and **Conclusion**. As an introductory part, **Chapter 1** provides the brief introduction of organic solar cells including polymer solar cell (PSC) and dye-sensitized solar cells (DSC) in the view point of operation principles and their patterning techniques for integrations. In **Chap. 2**, patterning technique for integration of organic solar cells, which is named a complementary transfer assisted lift-off (CTAL), is introduced. The fluororous-polymer, used as a sacrificial layer in CTAL technique, is also explained with their properties and patterning resolutions. The CTAL technique is applied to the hole transport layer of polymer solar cell and titania nanoparticles of dye-sensitized solar cell. The patterning resolution and reliability are also demonstrated. **Chapter 3 contains** the integrated solid-state DSCs with the patterned titania nanoparticle photoanode and the device characteristics using those layers. The titania nanoparticle photoanodes are well patterned in high resolution by CTAL technique. In order to integrate DSCs, solid-state hole transport materials instead of liquid electrolytes are used. It allows the cell to solve the leakage and corrosion problem as well as to be integrated. In **Chap. 4**, the solvent-dependent morphology of a conjugated polymer, poly(3-hexylthiophene) (P3HT) interfaced with [6,6]-phenyl-C61-butyric acid methyl ester (PCBM) and the evolution of the resulting inter-connected fibrillar structure (ICFS) in a diffusive bilayer heterojunction (DBHJ), is described. It is found that the fibrillar structure of the P3HT is preferentially developed in a

poor solvent and less soluble than an amorphous structure and the ICFS improves the power conversion efficiency significantly. Next, the integrated PSCs using CTAL technique are demonstrated. In integrated PSCs, the high performance such as high voltage and fill factor are achieved due to the reduced dark current. Finally, **Chapter 5** gives brief summary and some concluding remarks for our thesis.

## **Chapter 2. Complementary Transfer Assisted Lift-Off Techniques**

As described in the previous chapter, the shadow mask patterning and the ink-jet printing, which are the conventional method of depositing organic/inorganic materials, have shown critical problems in patterning high-resolution over large area. In this regard, the photolithography can be commonly used in both materials to improve the pattern resolution and reliability. In the case of vacuum process, thin films can be patterned by the combination of the photolithography and the following lift-off or etch processes in very high-resolution. However, the applicability of such photolithographic processes to the fabrication of organic electronic devices still remains uncertain because of the chemical incompatibility between the general solvents used in photolithography and organic materials.

In this chapter, I will provide a concept of a chemically stable/ compatible sacrificial layer assisted patterning method for organic electronic devices. According to the combination of the method for patterning sacrificial layer and lift-off technique, high resolution patterning process for organic/inorganic materials is provided. In detail, the thin films to be patterned are deposited on the entire substrate having the patterns of the sacrificial layer and then selectively lift-off leaving active area on a substrate. For the patterning of sacrificial layer, method of transfer printing, sort of softlithographic technique, is used.

At first, the material characteristics of fluoruous-polymer and fluoruous-solvent for the patterning process will be briefly introduced in **Chap. 2.1**. The methods of a transfer-printing for patterning of sacrificial layer will then be introduced in the viewpoint of the pattern ability and respective characteristics in the following section, and the patterns of two types of charge transport layer in organic solar cells are shown in the **Chap. 2.2** and **Chap. 2.3**, respectively.

## 2.1 Chemically Compatible Sacrificial Layer

Fluorous-solvents are perfluorinated or very highly fluorinated liquids, which are highly environmentally friendly, non-flammable and rarely toxic to humans. They also show zero ozone depletion potential as well as low global warming potential, which are well matched to the green energy industry. Moreover, the most important characteristics are that fluorous-solvent is typically immiscible with organic solvents and water, and they thus can satisfy the chemical orthogonality for processing general organic materials. In this regards, a kind of a fluorous-polymer (EGC-1700, 3M<sup>TM</sup> Novec), is chosen for a sacrificial layer, which can be well dissolved in a kind of hydrofluoroethers (HFE-7100, 3M<sup>TM</sup> Novec), one of highly fluorous-solvents, to guarantee the chemical compatibility.

Figures 2.1 and 2.2 show the chemical structures of fluorous-solvent, HFE-7100 and fluorous-polymer, EGC-1700, respectively. Tables 2.1 and 2.2 describe the general physical properties of HFE-7100 and EGC-1700, respectively.

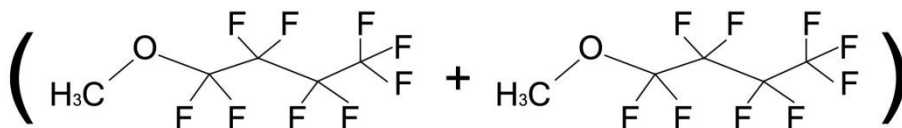


**Figure 2.1** The chemical structure of HFE-7100 (mixture of two isomers).

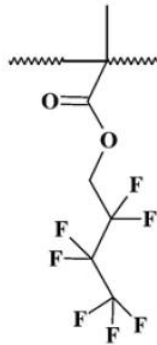


**Figure 2.2** The chemical structure of EGC-1700. (The schematic is taken from ref. [41]).

Note that this fluorous-polymer solution, HFE-7100, is comprised with fluorous-polymer which is very hydrophobic, and thus the sacrificial layer can be successfully applied to provide selective wettability as well. In addition, fluorous-polymer, EGC-1700 used as the sacrificial layer, can be easily formed on a variety of substrates including a glass, a metal foil, and even a plastic substrate, due to the very low (61 °C) boiling points of fluorous-solvent, by the method of dip-coating in a uniform thickness ranging from a few tens of nanometers to micrometer by simply varying the dip-coating speed and the solution concentration.

The use of a fluorous-polymer layer as a sacrificial layer is always possible provided two conditions are met. The first is that the fluorous-polymer layer can be easily patterned into fine features in a simple and cost-effective way. The other is that it can be clearly erased without any debris on a

**Table 2.1** The physical properties of HFE-7100.

| Properties                     | HFE-7100                                       |
|--------------------------------|--|
| Formula                        | C <sub>4</sub> F <sub>9</sub> OCH <sub>3</sub> |
| molecular weight               | 250  |
| boiling point                  | 61°C   |
| freeze point                   | -135°C   |
| liquid density                 | 13.6 (dyes/cm)                                 |
| Solubility of solvent in water | 12 ppmw  |
| Solubility of water in solvent | 95 ppmw  |
| Vapor pressure                 | 202 mmHg                                       |

**Table 2.2** The physical properties of EGC-1700.

| Properties                       | HFE-7100  |
|----------------------------------|---|
| appearance                       | clear, light-colored  |
| specific gravity @ 25°C          | 1.5   |
| Solvent                          | HFE-7100  |
| thermal stability of dry film    | repellent to chlorinated silicon oil<br>after 24 hrs at 175°C |
| surface energy of dry film       | 11 ~ 12 dynes/cm  |
| dielectric constant @ 25°C, 1kHz | 3.1   |
| coating thickness                | ~ 1 µm  |
| Refractive index of dry film     | 1.38  |

substrate. The latter can be easily achieved due to the material characteristics of chosen fluoros-polymer and solvent. The fluoros-polymer can simply be removed by adding a fluoros-solvent even after the formation of thin films. In this thesis, the transfer printing, one of the softlithographic techniques, is devised to provide appropriate way of patterning such fluoros-polymer layer.

## **2.2 Complementary Transfer Assisted Lift-Off**

### **2.2.1 Transfer-patterning of sacrificial layer**

Transfer-printing is one of the representative softlithographic techniques. From the general characteristics of softlithography, the transfer-printing can also provide a capability of high-resolution patterning, a large-area coverage, and an applicability even to curved surface. One of the attractive applications of transfer-printing is patterning of thin films to act as resists for following etch or lift-off processes. Transfer-patterning is particularly appealing to these systems since solvents used in traditional photolithographic processing can damage or degrade an organic layer or substrate. Thus, the transfer-patterning method can be reasonably applied to the patterning of sacrificial layer in our work. Such characteristics are essentially derived from the intrinsic nature of transfer-printing which is based on the work of adhesion. Figure 2.3 shows the basic concept of transfer-printing. A mold prepared for the desired pattern is coated with a film to be transferred. In our case, a fluorinated-polymer thin film was dip-coated on a predefined polydimethylsiloxane (PDMS) stamp. It is noted that a fluorinated-polymer solution was successfully dip-coated on a surface of a PDMS stamp. PDMS is well known to be very hydrophobic, and thus most solutions can hardly be coated without any surface treatment on a surface of a stamp. However, the EGC-1700 can be clearly coated on a hydrophobic surface with very high uniformity due to the use of highly volatile fluorinated-solvent, HFE-7100. The solvent rapidly evaporated before

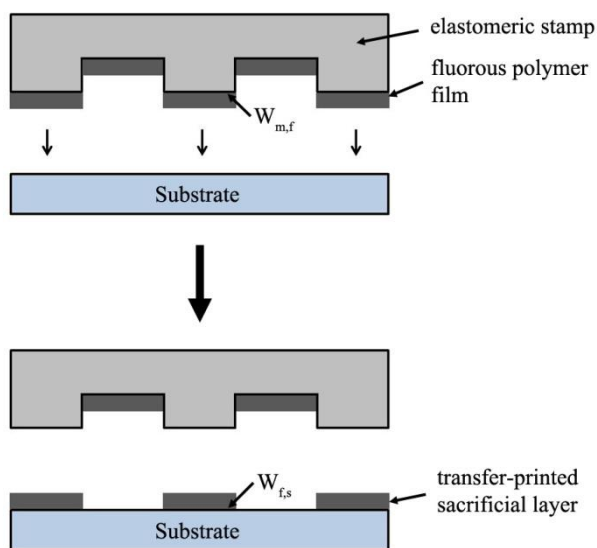


**Figure 2.3** Schematic diagram of the process of transfer-printing based on the work of adhesion.

the solution slips down from the surface of the PDMS mold, leaving the fluororous-polymer molecules on it, and the uniform thin film of sacrificial layer can consequently be formed. Then, the mold is brought into contact with a substrate to transfer a fluororous-polymer film from a mold to a substrate. Without any applied heat or pressure, intimate contact between the fluororous-polymer thin film and the substrate is spontaneously produced when the stamp placed on a substrate. When the mold is peeled-off, the film on the protruding parts of the mold gets transferred to the substrate. For this transfer to take place, the work of adhesion at the mold-film interface  $W_{m,f}$  has to be smaller than that at the film-substrate interface  $W_{f,s}$ .

Generally, the work of adhesion can be determined from contact angle measurement of two probe liquids on the substrate of interest [42, 43]. Based on the linearly additive nature of molecular forces, the work of adhesion  $W_{i,j}$  between two surfaces,  $i$  and  $j$ , is written as follows,

$$W_{i,j} = W_{i,j}^d + W_{i,j}^p, \quad (2.1)$$

where the dispersion and polar components are denoted by the superscripts  $d$  and  $p$ , respectively.

### **2.2.2 Sacrificial layer assisted lift-off**

Lift-off is a simple, easy method for patterning films that are deposited. In general lift-off is applied in cases where a direct etching of structural material would have undesirable effects on the layer below. One particular advantage of lift-off process is its ability to pattern with extremely high fidelity and for very fine geometries. However, the general solvent used in the lift-off process is hardly applied to the fabrication of organic electronic devices due to the chemical incompatibility for the most of organic materials.

Here, I introduced complementary transfer assisted lift-off (CTAL) technique for the patterning of charge transport layer in organic solar cell. For the transfer printing to directly produce the sacrificial layer patterns shown in Fig. 2.4, a fluororous-polymer solution was coated on the surface of an elastomeric stamp of PDMS having replica shapes of desired patterns and then transfer-printed onto the substrate. The SL patterns were well-defined by the intimate contact between the surfaces of the PDMS stamp and the

substrate surface under ambient conditions without any need to apply high heat/pressure as explained the previous section. Then, after blanket-deposition of organic/inorganic materials over the substrate having sacrificial layer patterns, the sacrificial layer was lifted-off in a fluoruous-solvent to leave out only the wanted patterns on a substrate. The general process of CTAL is shown in the Fig. 2.4. While the complicated photolithography process involving UV exposure or wet chemical etching/developing step is used in the traditional method, we can directly pattern the sacrificial layer without such c-

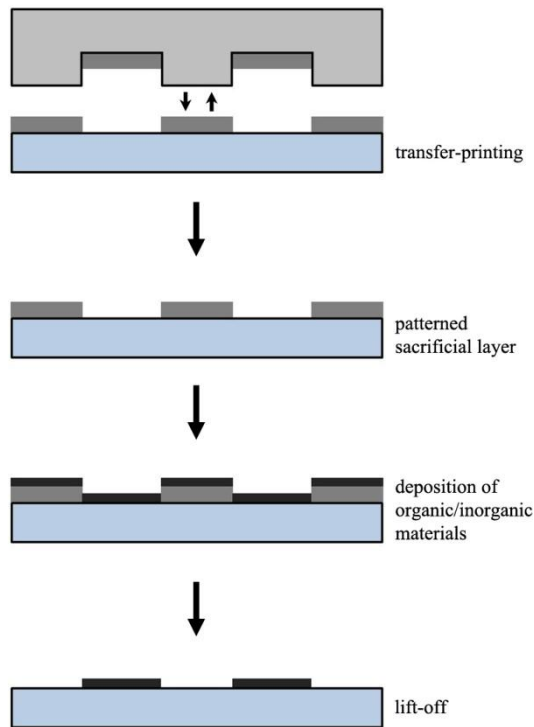


**Figure 2.4** Schematic diagram of the process of complementary transfer assisted lift-off technique.

omplex process by the method of a transfer-printing in a cost-effective way. It is important that the CTAL technique provides broad range of technical applicability.

Note that, the most important thing for the reliable lift-off process is the thickness of the sacrificial layer. When the sacrificial layer is not thick enough, the deposited film can also be deposited on the sidewall, standing upwards from the surface, and thus the films cannot be separated at the edge of the sacrificial layer. Such inadequate deposition may cause the fall over of target films on the surface of substrate during the lift-off process, leaving an unwanted shape on the substrate. Also, the sacrificial layer below the parts of a target film that should be lifted off may not be dissolved properly due to insufficient thickness of sacrificial layer. In this case, undesired parts of the target film will remain on the substrate. Therefore, in order to avoid possible defects or errors which may occur during the lift-off process, the sufficient thickness of the sacrificial layer should be satisfied. To control the thickness of sacrificial layer, the dip-coating speed and solution concentration were precisely varied, from 50 mm/min to 300 mm/min and from 2 % to 6 %, respectively. The thicknesses of transferred pattern are in the range of 50 nm to 400 nm.

Now, it is described that the pattern fidelity and the pattern resolution achieved in this patterning approach based on the transfer-printed sacrificial layer. In general, the feature resolutions of the patterns are governed by the complementary patterns of the sacrificial layer that were transfer printed using

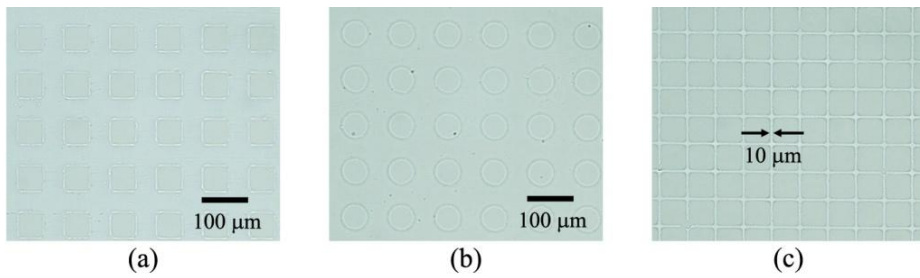


**Figure 2.5** The pattern examples of sacrificial layer films with various pattern features fabricated using transfer-printing.

a stamp. Moreover, the feature resolution of complementary patterns is equal to the resolution of soft-lithographic technique. Figure 2.5 shows three different types of patterns (squares, circles, net-like structures formed by lines) with different resolution ranging from 10 to 50  $\mu\text{m}$ . As shown in Fig. 2.5(a) and 2.5(b), a variety of patterns like square and circle were produced over the area of a few square centimeters. The feature resolution of 10  $\mu\text{m}$  can be easily achieved with complex shape and down to sub-micrometers depending on the pattern resolution of the stamp.

## **2.3 Patterning of Charge Transport Layer in Organic Solar Cells**

The CTAL patterning technique is successfully employed for fabricating pentacene-based thin-film transistors [44] and OLEDs [45] but it has not been explored for the OSCs with different classes of sensitive organic layers among a hole transport layer (HTL) and a heterogeneous layer composed of electron donor and electron acceptor in a stacked structure. In this section, I describe the patterning of charge transport layer in PSCs and DSCs. Using CTAL technique for the patterning of elements in OSCs, the integration of miniaturized OSCs can be produced in a single substrate.

### **2.3.1 TiO<sub>2</sub> patterning**

In DSCs, compact nanocomposite TiO<sub>2</sub> layer act as an electron transport layer. When the dye absorbs light, which is anchored to a wide bandgap TiO<sub>2</sub>, the photoexcited electrons transfer to the conduction band of TiO<sub>2</sub>. Then, TiO<sub>2</sub> carries the electron to the fluorine-doped tin oxide (FTO) electrode. For lateral integration of DSC cell in a small area, nanocomposite TiO<sub>2</sub> layer patterning in high resolution is the remaining challenge.

Here, I now describe the compact nanocomposite TiO<sub>2</sub> layer patterning using CTAL technique. Figure 2.6 shows the optical microscopic and the field emission scanning electron microscope (FE-SEM) (SU-70, Hitachi Co.)

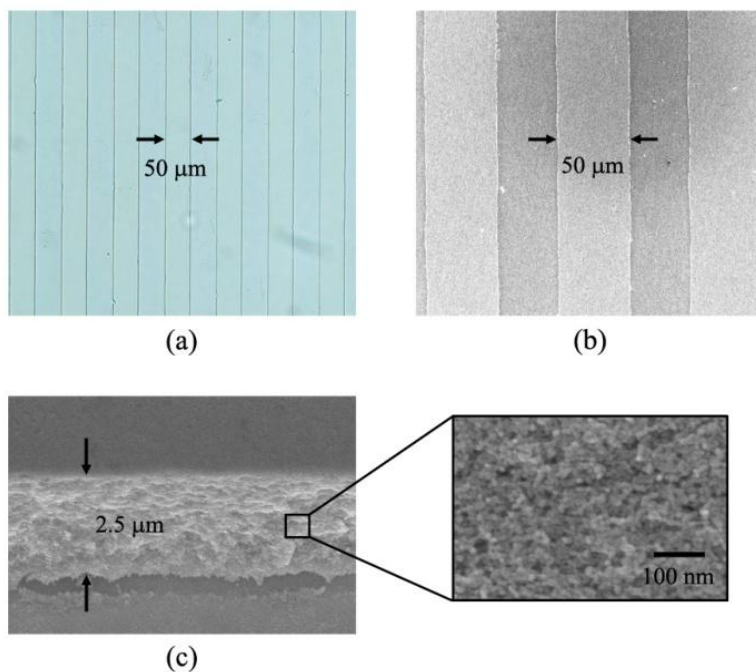


**Figure 2.6** (a) Optical microscopic and (b), (c) FE-SEM images of patterned  $\text{TiO}_2$  layer. The inset shows the FE-SEM image of the  $\text{TiO}_2$  nanoparticles in high resolution.

images of the patterned  $\text{TiO}_2$ . For producing patterned sacrificial layer, transfer-printing, described in previous section, was used. Nanoporous  $\text{TiO}_2$  electrodes were prepared from the colloidal Nanoxide-T paste (Solaronix) by doctor-blade techniques. For the solvent evaporation before the lift-off, the coated nanocomposite  $\text{TiO}_2$  film cured at  $50^\circ\text{C}$  for 3 min. Then, the  $\text{TiO}_2$  films were lifted-off with sacrificial layer by fluorous solvent. After that, the patterned films were annealed at  $450^\circ\text{C}$  for 30 min and cool down to room temperature the rate of  $100^\circ\text{C}/\text{h}$ . The resulting  $\text{TiO}_2$  film is around  $2.5 \mu\text{m}$

thick, as shown in the cross-sectional image of Fig. 2.6(c). The inset in Fig. 4 show the TiO<sub>2</sub> nanopaticles in the range of 15 ~ 20 μm.

In order to verify full evaporation of fluoruous-solvents in TiO<sub>2</sub> nanoparticle layer, FE-SEM and a solid fluorine-nuclear magnetic resonance (<sup>19</sup>F-NMR) spectrum were obtained on the titanium sample which are treated by fluoruous-solvent, annealed at 100°C for 2 h and 450°C for 30 min, as shown in Fig. 2.7 and Fig. 2.8. As shown in Fig. 2.7, fluoruous-solvent is not detected among the TiO<sub>2</sub> nanoparticles. It may be evaporated during annealing at 450°C for 30 min. It is noted that the fluoruous-solvent of HFE-7100 have very low boiling point of 61°C as shown in Table 2.1.

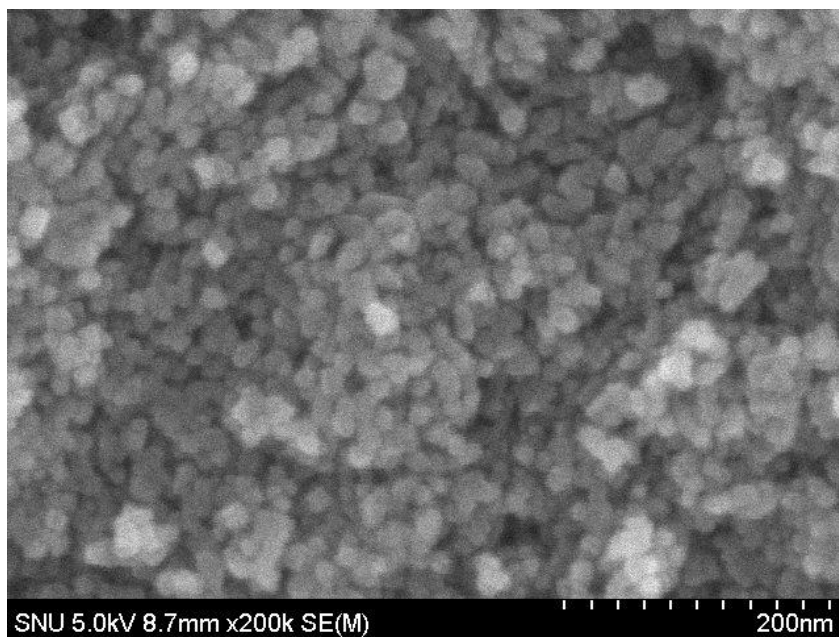


**Figure 2.7** High resolution FE-SEM images of TiO<sub>2</sub> layer after cutting.

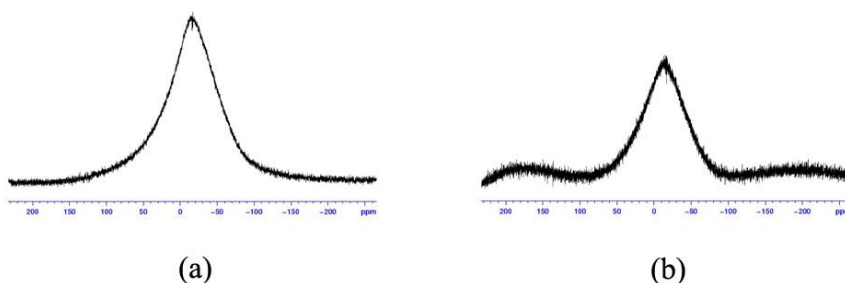


**Figure 2.8** Solid state  $^{19}\text{F}$ -NMR spectra of (a) empty rotor and (b)  $\text{TiO}_2$  nanoparticles after CTAL patterning which using fluoruous-solvent.

The solid  $^{19}\text{F}$  NMR spectra were recorded with a Bruker AVANCE II (500MHz) spectrometer with the 2.5 mm probe at the spin rate of 20 kHz. As shown in Fig. 2.8, there is no peak in the  $^{19}\text{F}$ -NMR spectrum of  $\text{TiO}_2$  nanoparticles. It is clearly demonstrated that fluoruous-solvent used in CTAL patterning is fully evaporated during the annealing of  $\text{TiO}_2$  layer.

### 2.3.2 $\text{MoO}_x$ patterning

A bulk heterojunction (HJ) PSC generally consists of a transparent anode, a bulk HJ active layer, and a cathode. Anode/cathode interfacial layer are used as charge selective contacts and charge transport between the bulk HJ layer and the electrodes. In general, poly(3,4-ethylenedioxythiophene) poly(styrenesulfonate) (PEDOT:PSS) is typically used as an anode interfacial layer. However, the PEDOT:PSS is hygroscopic and acidic with an associated reduction in device stability [46]. Recently, molybdenum oxide ( $\text{MoO}_x$ ) is studied as the promising alternative to PEDOT:PSS [46, 47]. For fabricating

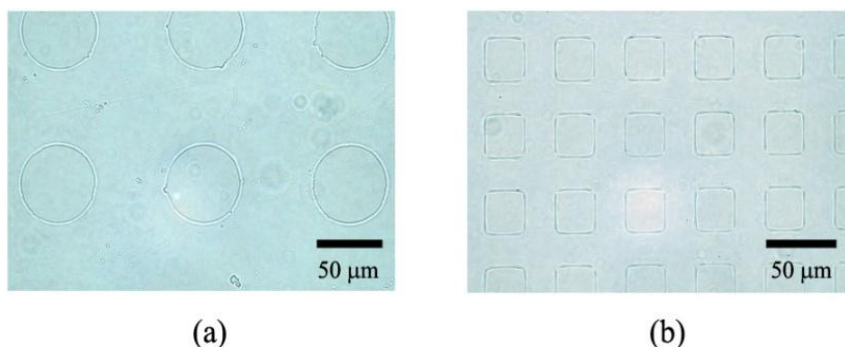


**Figure 2.7** Optical microscopic images of MoO<sub>3</sub> patterns showing (a) circles of 50 μm diameter and (b) squares of 25 μm in each side.

PSC array, the patterning technique for MoO<sub>3</sub> is required. Here, I describe the MoO<sub>x</sub> layer patterning using CTAL technique. First, sacrificial layer was transferred from PDMS to a substrate. Second, 30nm thick MoO<sub>x</sub> layer was thermally evaporated onto a substrate in a vacuum chamber at the deposition rate of 0.5 Å/s under the pressure of about  $5 \times 10^{-6}$  Torr. Third, for lifting-off the MoO<sub>3</sub> layer on the sacrificial layer to leave only wanted regions, the substrate was immersed in the fluorine solvent for 30 seconds. Then, the regions covered with the sacrificial layer were removed and only the wanted regions were left on the substrate. Figure 2.7 shows the optical microscopic images of MoO<sub>x</sub> patterns showing circles of 50 μm diameter and squares of 25 μm in each side. The pattern size can be down to a few micrometer according to the resolution of a PDMS stamp used, and even to a sub-micrometer scale with the use of rigiflex stamp, which is flexible yet rigid, to pattern more precise patterns of hydrophobic sacrificial layer.

# Chapter 3 Integration of Solid-state Dye-sensitized Solar Cells

## 3.1 Introduction

Dye-sensitized solar cells (DSCs) have attracted great attention as one of the promising photovoltaic technologies, both for their low cost materials and high power conversion efficiencies [20, 48]. Liquid electrolyte-based DSCs have shown efficiencies surpassing 11% [49, 50]. However, these liquid-based DSCs suffer from potential leakage and corrosion problems, and more generally, permeation of water or oxygen molecules and their reaction with the electrolytes may worsen the cell performance [27, 51]. Recently, an effective approach to solve such a problem by replacing the volatile liquid electrolyte with solid-state hole transport materials (HTMs) is researched [26, 28, 52-55].

For the practical use in applications of real power generation and usage as a power source, the integration of DSC arrays in high resolution is one of the most critical issues to be further explored. However, in spite of much effort in efficiency enhancements of single DSC device, the integration of DSCs has not been researched yet. It may be attributed to the patterning difficulties of  $\text{TiO}_2$  photo-electrode. In solid-state DSCs (ss-DSCs), the optimized film thicknesses of  $\text{TiO}_2$  photo-electrode for efficient charge collection are 2~2.5

$\mu\text{m}$  [52]. Note that, existing  $\text{TiO}_2$  patterning methods of wet etch using HF solution and  $\text{SF}_6/\text{Ar}$  plasma etch are complex, inefficient, and have limits in micrometer scale pattern to  $\text{TiO}_2$  thick film [56, 57]. The imprinting method is applied to pattern  $\text{TiO}_2$  films but the patterns are formed only a few hundred nanometer thick in a surface area [37, 58].

In this work, I developed integrated ss-DSCs on a single substrate by micropatterning of  $\text{TiO}_2$  using CTAL patterning as shown in Fig. 3.1. The  $\text{TiO}_2$  pattern in micro-scale by CTAL patterning and the use of solid-state hole transport materials make the possibility of integrated solar cells.

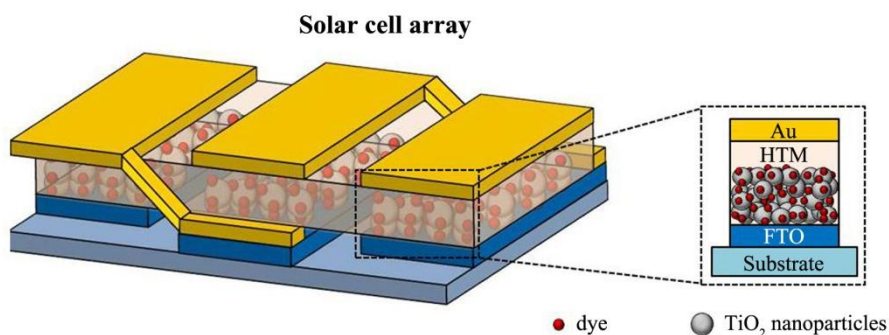


**Figure 3.1** Schematic diagram of the solid-state DSC array. Solid-state DSC comprised of transparent FTO on glass, nanoparticle photoanode of  $\text{TiO}_2$  covered in a monolayer of sensitizing dye, hole transport material for solid-state electrolyte, and gold back electrode.

## **3.2 Fabrication Process of Solid-State Dye-Sensitized Solar Cell Array**

### **3.2.1 TiO<sub>2</sub> patterning technique**

Our ss-DSC array with patterned TiO<sub>2</sub> photo-electrode is shown in Fig. 3.1. First, the fluorine-doped tin oxide (FTO) prepatterned glass substrate was cleaned sequentially with acetone, deionized water and ethanol in an ultrasonicator for 10 min each step, and then dried with nitrogen gas. The cleaned substrates were dried at 90°C in a vacuum oven for 10 min to remove any residual water. The dried FTO glass is cleaned out by the treatment of ultraviolet-ozone for about 5 min. The cleaned FTO glass is immersed in 40 mM TiCl<sub>4</sub> aqueous solution at 70°C for 30 min. The TiCl<sub>4</sub> treated FTO glass is cleaned by above sequential process. For fabricating the patterned TiO<sub>2</sub> on the FTO, the CTAL patterning using hydrophobic sacrificial layer (SL) was used as shown in Fig. 3.2. A SL used in this study is fluorous polymer (3M Novec<sup>TM</sup> EGC-1700) which can be dissolved in a highly fluorous solvent (3M Novec<sup>TM</sup> HFE-7100). Note that the fluorous solvent is chemically inert to most of organic and inorganic materials, and is thus definitely able to be used in the process for PSCs [44, 45]. For the transfer printing to produce the SL patterns, a fluorous polymer solution was coated on the surface of an elastomeric stamp of poly(dimethylsiloxane) (PDMS) having replica shapes

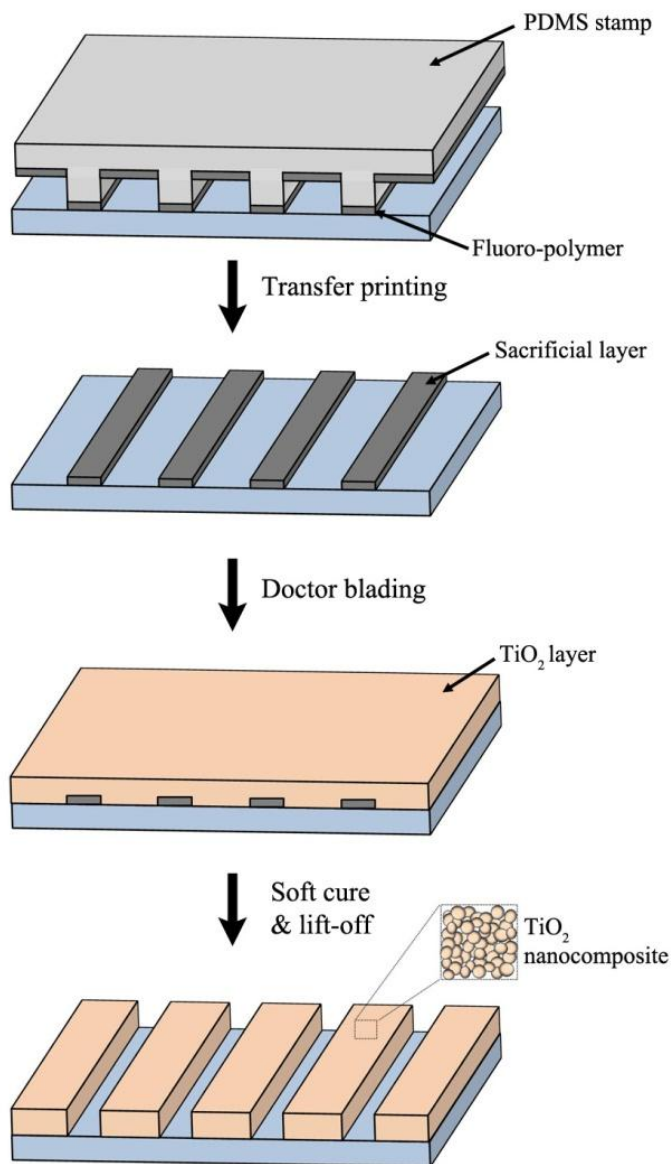
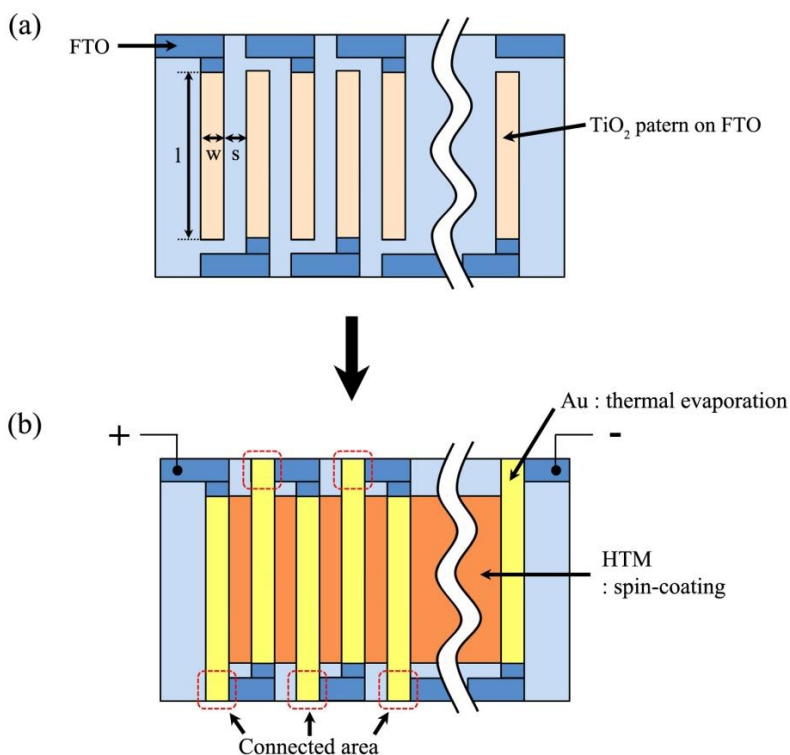


**Figure 3.2** Schematic diagram of the solid-state DSC array. Solid-state DSC comprised of transparent FTO on glass, nanoparticle photoanode of  $\text{TiO}_2$  covered in a monolayer of sensitizing dye, hole transport material for solid-state electrolyte, and gold back electrode.

of desired TiO<sub>2</sub> patterns and then transfer-printed onto the FTO substrate, shown in the Fig. 3.2. The SL patterns on PDMS stamp were easily transferred to the substrate without any additional treatment such as heat and/or pressure due to the low surface energy of the PDMS stamp compared to that of the glass substrate. Then, 2.5 μm thick TiO<sub>2</sub> photo-electrodes were prepared on the SL patterned FTO substrates from Ti-Nanoxide T (Solaronix SA) paste by a doctor blade method. The TiO<sub>2</sub> film was soft-cured at 50°C for 3 min on a hotplate. After soft-curing, the SL was lift-off in a fluoruous solvent to leave out only the TiO<sub>2</sub> on FTO active regions. The patterned TiO<sub>2</sub> layer were annealed at 80°C for about 2 h and slowly heated to 450°C and annealed at this temperature for 30 min.

### **3.2.2 Fabrication process of solar cell array**

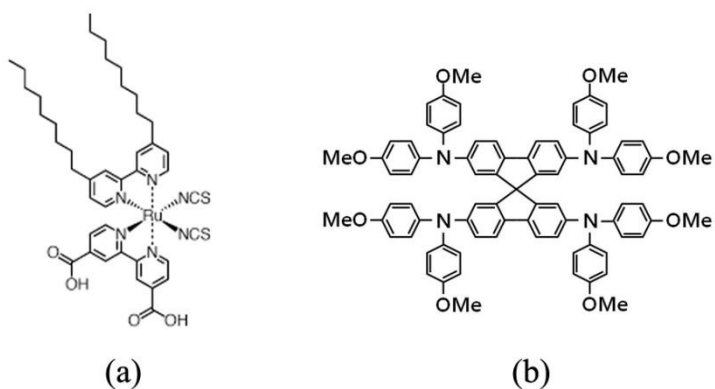
Figure 3.3 shows the plan view of the complete device composed of single cells in series interconnections. For fabricating DSC array, TiO<sub>2</sub> film was patterned on FTO having a geometry shown in Fig. 3.3(a) by CTAL patterning technique. The prepared TiO<sub>2</sub> film was soaked in 3 mM of 1:1 mixture of acetonitrile and *tert*-butyl alcohol solution with Z907 dye (Solaronix SA) for 24 h. For efficiency measurements, the electrodes were placed for 10 minutes un a 6 mM Z907 and 4-guanidinobutyric acid (Sigma-Aldrich) as coabsorbent in a 1:1 mixture in 1-methoxy-2-propanol solution (Sigma-Aldrich) [59]. The dye coated patterned TiO<sub>2</sub> film was briefly rinsed in acetonitrile and dried in air for a minute. The HTM of spiro-OMeTAD (American Dye Source) was



**Figure 3.3** Schematic diagram of the solid-state DSC array. Solid-state DSC comprised of transparent FTO on glass, nanoparticle photoanode of TiO<sub>2</sub> covered in a monolayer of sensitizing dye, hole transport material for solid-state electrolyte, and gold counter electrode.

prepared by dissolving 200 mg/mL in chlorobenzene solution by heating and stirring at 70°C for 1 h. The lithium bis(trifluoromethylsulfonyl)imide salt (Li-TFSI) ionic dopant dissolved in acetonitrile at 170 mg/mL, was added to the spiro-OMeTAD solution at a ratio of 15  $\mu$ L Li-TFSI solution: 72 mg of spiro-OMeTAD. For efficiency measurements, 4-tert-Butylpyridine (TBP) was added to the solution with at a ratio of 7  $\mu$ L TBP: 72 mg spiro-OMeTAD

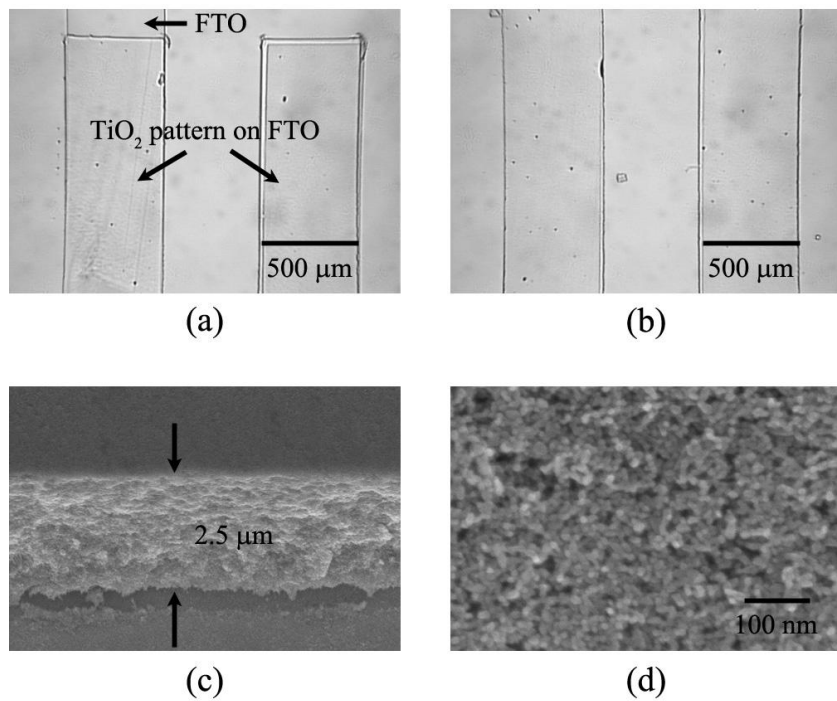
[27, 51]. The solution was dropped onto the TiO<sub>2</sub> patterned FTO glasses and left 1min before spin coating at a rate of 2000 rpm at room temperature. Prior to spin coating, the mesoporous TiO<sub>2</sub> films are filled with solution by capillary action. For the counter metal electrode, a gold (Au) layer of 100 nm thick was applied by thermal evaporation at the rate of 1 Å/s in a vacuum chamber. The final configuration is array of 20 PSCs in series, with a length (l) of 1.4 cm and the same value of widths (w) and spaces (s) is 500 μm as shown in Fig. 3.3(a) and 3.3(b). A total cell area was 1.4 cm<sup>2</sup>. The chemical structures of Z907 dye and spiro-OMeTAD are illustrated in Fig. 3.4 [60, 61]. The photocurrent was measured under illumination from a solar simulator with AM 1.5G filters whose light intensity was calibrated with a standard silicon diode. The current-voltage characteristics were obtained using a source-measure unit (Model 2400, Keithley).



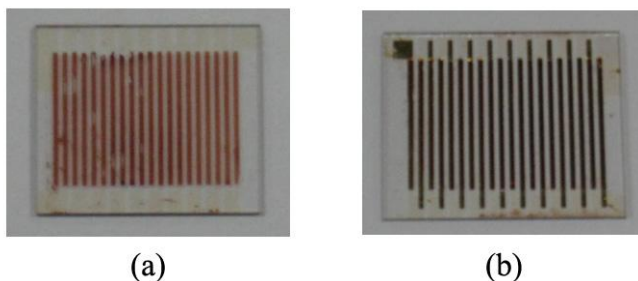
**Figure 3.4** Chemical structures of (a) Z907 dye [60] and (b) spiro-OMeTAD [61].

### 3.3 Patterned TiO<sub>2</sub> Film in Micrometer Scale

Figure 3.5 shows the optical microscopic and the field emission scanning electron microscope (FE-SEM) (SU-70, Hitachi Co.) images of the patterned TiO<sub>2</sub>. As shown in Fig. 3.5(a) and 3.5(b), the patterned TiO<sub>2</sub> film by CTAL patterning are well-aligned onto the FTO active area. The resulting patterned TiO<sub>2</sub> film is around 2.5 μm thick, as shown in the cross-sectional image of



**Figure 3.5** (a) Optical microscopic and (b)~(d) FE-SEM images of patterned TiO<sub>2</sub> layer. (c) The cross-sectional image of TiO<sub>2</sub> film. (d) The enlarged image of TiO<sub>2</sub> film composed of the TiO<sub>2</sub> nanoparticles.



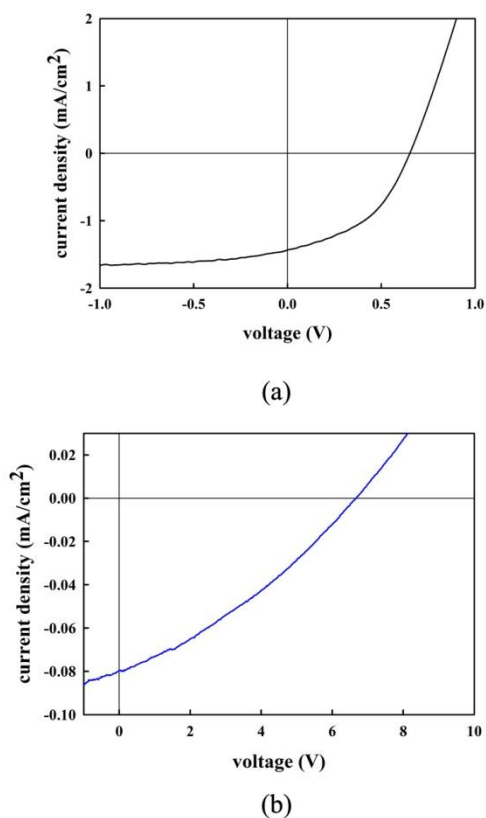
**Figure 3.6** (a) Dye adsorbed nanocrystalline TiO<sub>2</sub> film of 20 array. (b) Fabricated ss-DSC array after spin-coating of spiro-OMeTAD and gold deposition.

Fig. 3.5(c). This thickness is similar to the optimized TiO<sub>2</sub> film thickness in ss-DSCs as mentioned above. Figure 3.5(d) shows enlarged image of TiO<sub>2</sub> film composed of the TiO<sub>2</sub> nanoparticles in the range of 15 ~ 20  $\mu\text{m}$ .

Figure 3.6(a) shows the patterned TiO<sub>2</sub> array with dye adsorption. Figure 3.6(b) shows fabricated 20 DSC array with a total length of 2.0 cm and width of 2.4 cm, as illustrated in Fig. 3.3(b).

### 3.4 Solar Cell Characteristics

Figure 3.7 shows the current-voltage curves of single and 20 ss-DSC array under the AM 1.5 100mW/cm<sup>2</sup> illumination. As shown in Fig. 3.7(a), single ss-DSC with HTM of spiro-OMeTAD gave an open-circuit voltage ( $V_{oc}$ ) of 0.65 V, a short-circuit current density ( $J_{sc}$ ) of 1.44 mA/cm<sup>2</sup>, a fill factor (FF) of 0.44, and a power conversion efficiency (PCE) of 0.41%. In the 20 ss-DSC



**Figure 3.7** The current-voltage curves of (a) single and (b) 20 ss-DSC array under the AM 1.5 100mW/cm<sup>2</sup> illumination.

arrays, the highest  $V_{oc}$  of 6.68 volts and the fill factor (FF) of 0.32 were achieved from the ss-DSC array with patterned  $TiO_2$  layer as shown in 3.7(b). The low PCE of ss-DSC array may be due to the low FF. The FF difference between the single and array is due to the 20 FTO- $TiO_2$  and HTM-metal junctions, causing the increase of series resistance ( $R_s$ ). The  $R_s$  derived by the slope of the plot of  $dV/dI$ , when  $I = 0$  [62]. The values of  $R_s$  derived from single and 20 array cells are  $150 \Omega cm^2$  and  $5.52 \times 10^6 \Omega cm^2$ . The characteristics of the ss-DSC array, such as the  $V_{oc}$ ,  $J_{sc}$ , FF, and PCE were summarized in Table 3.1.

**Table 3.1** The values of  $J_{sc}$ ,  $V_{oc}$ , FF, and PCE in single and 20 ss-DSC array devices.

| ss-DSC devices | $J_{sc}$ (mA/cm <sup>2</sup> ) | $V_{oc}$ (V)    | FF              | PCE (%)         |
|----------------|--------------------------------|-----------------|-----------------|-----------------|
| single         | $1.44 \pm 0.13$                | $0.65 \pm 0.01$ | $0.44 \pm 0.02$ | $0.41 \pm 0.05$ |
| 20 arrays      | $0.79 \pm 0.06$                | $6.68 \pm 0.05$ | $0.32 \pm 0.03$ | $0.17 \pm 0.04$ |

### **3.5 Summary**

I developed a patterning technique based on CTAL patterning to produce high resolution integrated ss-DSC arrays. The SL patterns complementary to the active patterns can be generated by the transfer printing. By transfer printing of SL patterns, TiO<sub>2</sub> film of 2.5 μm thick is patterned simple and cost-effective method. The fabricated ss-DSC array shows 6.68 V in 20 series connected cell. This generic patterning platform is expected to be applicable for constructing integrated ss-DSCs in a cost-effective way.

## **Chapter 4. Polymer Solar Cells**

### **4.1 Efficiency Enhancement of PSCs in a Bilayer Configuration**

#### **4.1.1 Introduction**

Organic PV devices based on conjugated polymers have attracted great interest as a class of alternatives to inorganic PV devices because of low cost, easy processing, light weight, and mechanical flexibility [63-66]. In order to enhance the  $\eta_p$  of polymer PV devices, there are two major issues; one is to manipulate an interface between a donor layer and an acceptor layer for the exciton generation to be located within the range of the exciton diffusion length (about 10 nm) [63, 64] and the other concerns spatially uninterrupted pathways for the charge carriers after the exciton dissociation. Recently, a variety of diffusive bilayer heterojunctions (DBHJ) that have relative advantages of a bilayer heterojunction (HJ) and a bulk HJ have been demonstrated to enlarge the donor-acceptor interface and to produce the uninterrupted carrier pathways toward the corresponding electrodes [67-79]. The simplest approach to the construction of the DBHJ is based on the sequential spin-coating of a solution of a donor material and a solution of an acceptor material [67-73]. The diffusive nature of the donor-acceptor interface

is then produced by randomly dissolving the first layer during the second spin-coating process. In this approach, the lamination technique [74] or thermal treatment [75-79] is known to be useful for creating percolation paths in a bilayer HJ but it often leads to a low value of  $\eta_p$  due to the formation of the diffusive interface at a molecular level but not a domain level of the donor and the acceptor.

In bulk HJ devices based on conjugated polymers (electron donors), the fibrillar structures of the polymers were found to improve the carrier mobility and the power conversion efficiency [80-87]. This suggests that the structural arrangement of the polymer chains and the crystallinity are important factors to understand the physical mechanism for the enhancement of the power conversion efficiency in view of the fibrillar morphology in the polymer-based DBHJ. It is expected that the fibrillar morphology and the formation of inter-diffusive regions depend on the nature of the solvent being used, for example, whether it is good or poor, polar or nonpolar, and the boiling temperature is low or high.

In this work, I present the solvent-dependent morphological structure as well as the evolution of an inter-connected fibrillar structure (ICFS) of a conjugated polymer, poly(3-hexylthiophene) (P3HT), interfaced with [6,6]-phenyl-C61-butyric acid methyl ester (PCBM) in a DBHJ PV device. It is found that the solubility of the P3HT plays an important role on the formation of the fibrillar morphology of the P3HT which is critical for producing interpenetrating networks at a domain level through partial dissolving. When a poor solvent was used,  $\eta_p$  was enhanced by a factor of five compared to a

good solvent whose boiling temperature ( $T_b$ ) is similar to that of the poor solvent. Due to the difference in the solubility between the amorphous and fibrillar structures in the P3HT layer, an interpenetrating fibrillar structure with the acceptor layer was spontaneously formed during the subsequent spin-coating process.

#### **4.1.2 Fabrication process of PSCs with inter-connected fibrillar structures**

Our PV device with the P3HT (an electron donor) and the PCBM (an electron acceptor) in the DBHJ configuration is shown in Fig. 4.1(a). Indium-tin-oxide (ITO) was used for a transparent anode. The ITO coated glass substrate was cleaned sequentially with acetone, isopropyl alcohol, and methyl alcohol in an ultrasonicator for 10 min each. At each cleaning step, the substrate was rinsed with deionized water for 5 min in an ultrasonicator and purged with nitrogen gas. The cleaned substrates were dried at 90 °C in a vacuum oven for 10 min to remove any residual water. The ITO substrate was modified with a hole transport material of poly(3,4-ethylenedioxylenethiophene)-polystyrene sulfonic acid (PEDOT:PSS, PVP AI 4083, Baytron P) to prepare a hole transport layer of 40 nm thick. A diffusive or an interpenetrating interface was then produced with the P3HT and the PCBM as shown in Fig. 4.1(b) in the DBHJ device. In principle, two types of the interfacial regions, one of which is composed of inter-diffusive structures

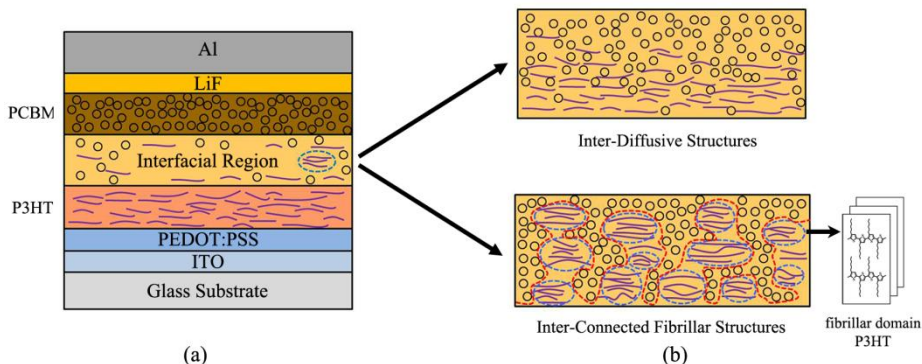


**Figure 4.1** Schematic diagram showing the cross-section of (a) an organic PV device with the DBHJ active layer. (b) Possible types of interfacial regions; inter-diffusive structures (IDS) and inter-connected fibrillar structures (ICFS).

(IDS) at a molecular level [74-79] and the other is inter-connected fibrillar structures (ICFS) at a domain level, may be formed as shown in Fig. 4.1(b). The power conversion efficiency of the BHJ PV device would depend on the relative portions of the two structures. Note that as shown in Fig. 4.1(b), the ICFS thickness is similar to the P3HT film thickness since the fibrillar structure is initially developed throughout the whole P3HT film.

Since a high molecular weight (MW)-P3HT polymer prefers to form a fibrillar structure which is less soluble than an amorphous structure [80, 81], I used a high MW-P3HT (the average  $M_w = 87000$ , Sigma-Aldrich). Four different solvents of *p*-xylene (PX) ( $T_b = 138^\circ\text{C}$ ), chlorobenzene (CB) ( $T_b = 132^\circ\text{C}$ ), dichlorobenzene (DCB) ( $T_b = 180^\circ\text{C}$ ), and chloroform (CF) ( $T_b = 61.5^\circ\text{C}$ ) were used for dissolving the P3HT to examine how the nature of the solvent (or the solubility of the P3HT) and  $T_b$  influence the morphology and

the crystallinity of the P3HT in a solid film prepared from a solution. Note that the PX and the CB have similar  $T_b$ 's while the DCB has a higher  $T_b$  and the CF has a lower  $T_b$  than the PX. The PX is a poor solvent with relatively low solubility compared to other solvents. At room temperature, the P3HT is slightly soluble in the PX and optically opaque whereas it is fully dissolved in a good solvent (the CB, the DCB, or the CF) and transparent. At 80°C, however, the P3HT in the PX is substantially dissolved and the aggregation of polymer chains occurs during cooling down to room temperature [82]. Three solutions were prepared by dissolving 3 wt.%, 3 wt.%, and 2 wt.% of the P3HT in the CB, the DCB, and the CF, respectively. These three solutions were spin-coated at 3000 rpm onto the PEDOT:PSS-coated ITO glasses at room temperature while the P3HT solution (1.5 wt.%) in the PX was spin-coated at 1000 rpm to maintain the same thickness as other three cases. For all the cases, the thickness of the P3HT layer was determined to be about 70 nm. On the top of each P3HT layer, the PCBM solution (1.5 wt.% in the PX) was spin-coated at 1000 rpm to construct an active layer in the BHJ configuration. The overall thickness of each PCBM-on-P3HT film was found to be about 100 nm.

For the back metal electrode (cathode), a lithium fluoride (LiF) layer of 0.5 nm thick and an aluminum (Al) layer of 100 nm thick were successively prepared by thermal evaporation at the rate of 1 Å/s in a vacuum chamber. Note that the photoactive area of our solar cells was 0.09 cm<sup>2</sup>. The surface morphologies of the P3HT layers and the PCBM-on-P3HT films were observed using an atomic force microscopy (AFM) (XE-150, PSIA).

Structural information about the P3HT layer was deduced from the data of grazing incidence x-ray diffraction (GIXRD) (D8 DISCOVER, Bruker) using a synchrotron x-ray beam with the wavelength  $\lambda = 0.154056$  nm. The UV-visible absorption spectra were measured using a spectrometer (V-530, Jasco). The photocurrent was measured under illumination from a solar simulator with AM 1.5G filters whose light intensity was calibrated with a standard silicon diode. The current-voltage characteristics were obtained using a source-measure unit (Model 2400, Keithley).

### **4.1.3 Solvent-dependent fibrillar morphologies of polymer**

#### ***Morphological properties of P3HT layers***

I first examine how the surface morphology of the P3HT layer is affected by the type of the solvent used. Figure 4.2 shows the AFM images and the corresponding morphological profiles of the P3HT films for four different solvents. For the P3HT layer prepared from the PX, the fibrillar structures mixed with the amorphous structures were formed as shown in Fig. 4.2(a) while for the P3HT layers from the CB, the DCB, and the CF, no fibrillar structures were microscopically observed as in Fig. 4.2(b), Fig. 4.2(c), and Fig. 4.2(d), respectively. The average values of the root-mean-square roughness of the P3HT layer for the PX, CB, DCB, and CF were found to be 4.37, 2.76, 5.24, and 0.91 nm, respectively. The smallest surface roughness was obtained for the CF case whereas the largest for the DCB case. This suggests that the surface roughness is also influenced by the boiling temperature

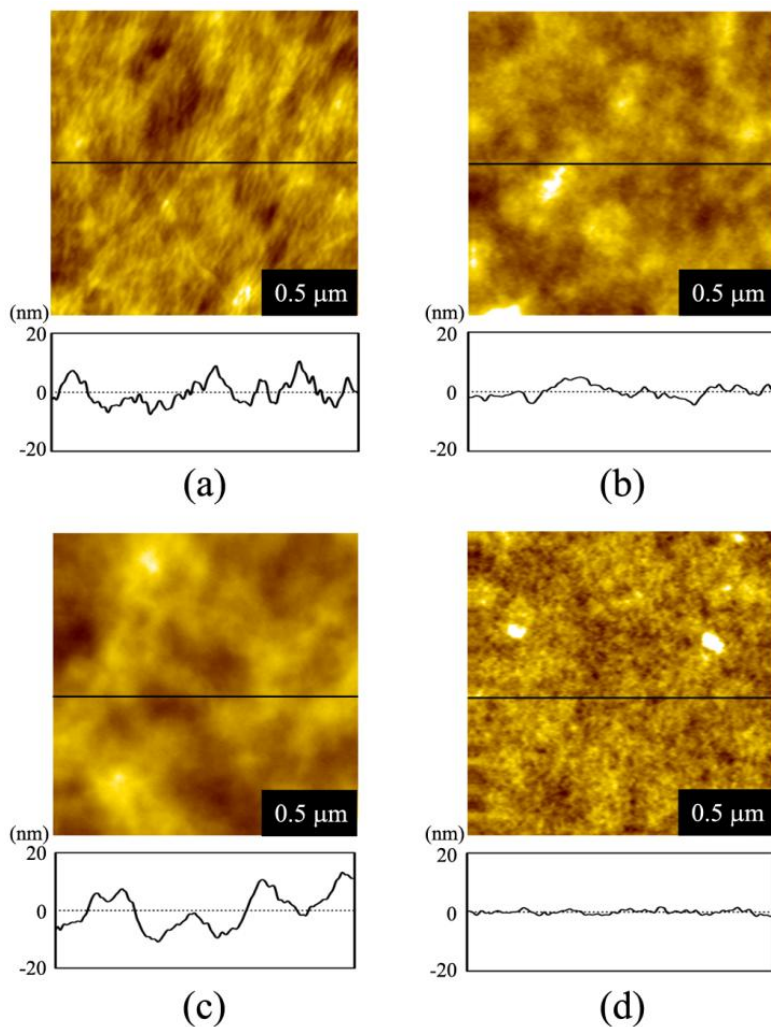


**Figure 4.2** The AFM images and the corresponding morphological profiles of the P3HT layers prepared from four different solvents: (a) the PX, (b) the CB, (c) the DCB, and (d) the CF. The AFM images were obtained with scanning an area of 1.5 μm x 1.5 μm. Morphological profiles were obtained along the black lines in the AFM images.

( $T_b = 61.5^\circ\text{C}$  for the CF) in addition to the presence of the fibrillar structures. The fibrillar morphology is an indicative of the structural ordering of the P3HT chains. Each fibril consists of  $\pi$ -stacked chains with the backbone axis which lies along the stacking direction in a lamellar structure [81, 82]. It is noted that the poor solubility of the P3HT prefers to spontaneously form nanofibers as clearly seen in Fig. 4.2(a). The typical length of a nanofiber is in the range from 0.2 to 0.5  $\mu\text{m}$ , the thickness from 5 to 15 nm, and the width from 15 to 50 nm [82, 83]. For a solvent with good solubility such as the CB or the DCB, the polymer chain of the high MW-P3HT tends to adopt a coil-like, disordered conformation in solution [88]. This implies that the nanofiber structure of the P3HT will not be energetically favored in a good solvent.

Figure 4.3(a) shows the GIXRD data for the P3HT layers prepared from three different solvents (the PX, the CB, and the DCB) and those for the bare substrate. Note that the CF case is not likely to produce the fibrillar structure as in Fig. 4.1(b). The x-ray intensity was obtained by  $2\theta$  scan for fixed angle of grazing incidence [89]. The grazing angle was chosen to be  $0.5^\circ$  which is slightly larger than the critical angle for total reflection so that the x-ray intensity comes mostly from the P3HT surface. The primary (100) diffraction peaks for the P3HT layers prepared from the PX, the CB, and the DCB were occurred at  $2\theta = 5.37^\circ$ ,  $5.25^\circ$ , and  $5.30^\circ$  respectively. Note that for the CF case, essentially no diffraction peaks were observed since the lamellar ordering of the P3HT was barely formed. The diffraction data for the CF were

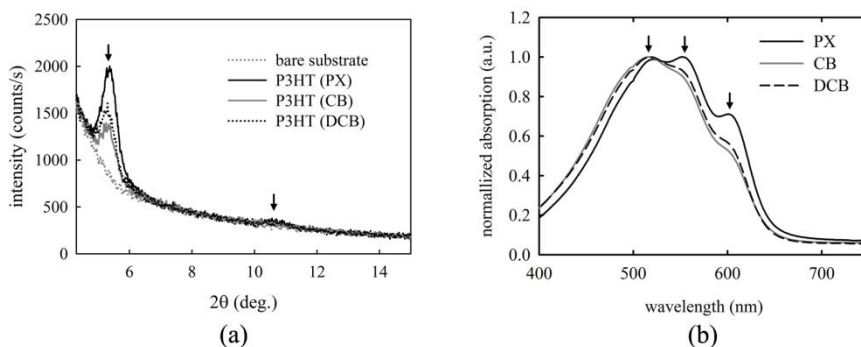


**Figure 4.3** (a) The out-of-plane GIXRD diffractograms for the incident angle of  $0.5^\circ$  and (b) the UV-visible absorption spectra of the P3HT layers prepared with different solvents.

similar to those for the bare substrate. From Bragg's law,  $2d\sin\theta = m\lambda$  with a positive integer  $m$  representing the interference order, the corresponding lattice constant  $d$  was obtained to be  $16.4 \text{ \AA}$  for the PX,  $16.8 \text{ \AA}$  for the CB, and  $16.7 \text{ \AA}$  for the DCB. These values are in the range of the lattice parameter of the P3HT in a lamella structure [86] of the out-of-plane orientation with the backbone parallel to the substrate surface and the side-chains perpendicular to it [83]. Considering the secondary peak observed at  $2\theta = 10.7^\circ$ , the P3HT film only from the PX exhibits the large structural order associated with the lamella stacking. This is consistent with the AFM images showing the fibrillar structures of the P3HT in Fig. 4.2(a). In other words, the lamellar ordering of the P3HT is profound and grows into a fibrillar structure on a macroscopic scale in a poor solvent (the PX) while it exists locally in a good solvent (the CB or the DCB). Moreover, our experimental results indicate that for good

solvents, the degree of the local lamellar order depends on the boiling temperature to some extent.

Figure 4.3(b) shows the UV-visible absorption spectra of the P3HT layers that were spin-coated from three solutions in the PX, the CB, and the DCB. For the P3HT layer from the PX, three absorption peaks were clearly identified at around 521 nm, 552 nm, and 601 nm in our case. Among them, the peak at around 601 nm comes from the interchain transition [90] of P3HT in ordered aggregates associated with  $\pi$ - $\pi^*$  stacking [83, 91, 92]. The other two peaks at around 552 nm and 521 nm are related to the structural arrangement of the chain segments or the effective conjugation lengths of the P3HT in the solid state [90]. The peak intensities at around 601 nm in the PX, the CB, and the DCB cases suggest that the P3HT layer from the PX is more ordered than the others. This is in good agreement with the AFM and the GIXRD results in Fig. 4.2 and Fig. 4.3, respectively. In addition, the red-shift of the peak at 516 nm (the CB) to 518 nm (the DCB) and 521 nm (the PX) indicates the increase of the effective conjugation length in the P3HT layer [90]. This means that the solvent property plays an important role in the structural ordering of the P3HT.

### ***Solvent-annealing effect on morphological changes of PCBM-on-P3HT films***

I first investigate the solvent-annealing (SA) effect on the morphological changes of two P3HT layers, the PX-P3HT layer prepared from the PX and the DCB-P3HT layer from the DCB, before processing the subsequent PCBM layer from a solution in the PX. For the study of the

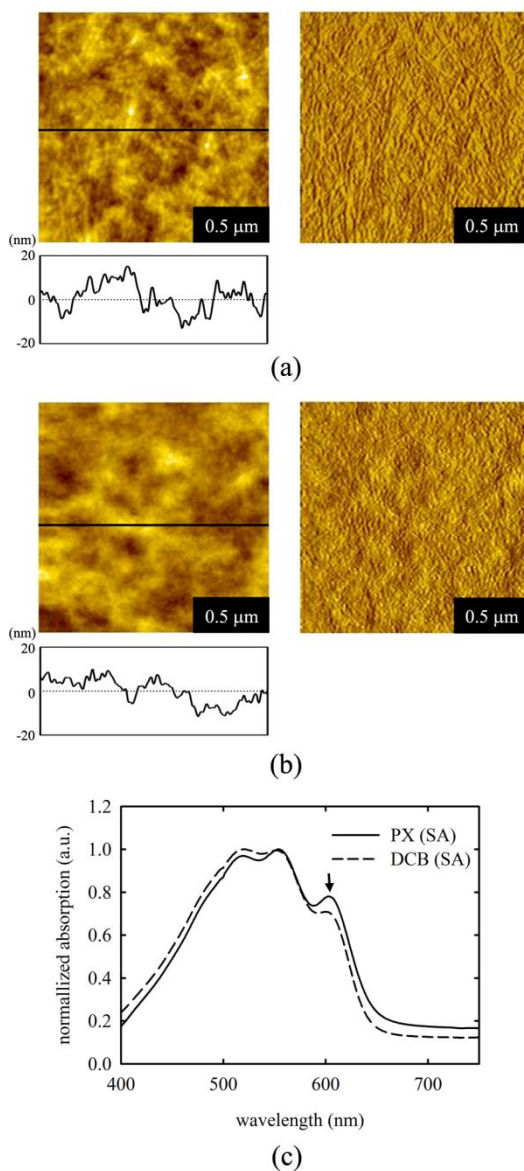


**Figure 4.4** The AFM images and the corresponding morphological profiles of the P3HT layers prepared from (a) the PX and (b) the DCB after the solvent annealing with the PX: The left column shows the amplitude images and the right column shows the phase images. Morphological profiles were obtained along the black lines in the amplitude images. (c) The UV-visible absorption spectra of (a) and (b).

solvent-annealing (SA) effect itself, the two P3HT layers were independently treated with the PX which is the solvent for the PCBM. Figures 4.4(a) and 4.4(b) show the AFM images (the amplitude image in the left and the phase image in the right) and the UV-visible absorption spectra of the PX-P3HT and the DCB-P3HT layers treated with the PX, respectively. The corresponding morphological profiles of the two P3HT layers were shown in the bottom. The average value of the root-mean-square roughness of the PX-P3HT layer and that of the DCB-P3HT layer were about 5.68 nm and 6.42 nm, respectively. The surface roughness of the P3HT layer treated with the PX was increased by about 2 nm compared to that of the untreated P3HT layer. This may be attributed to the solvent-annealing (SA) effect by the PX which results in the increase of ordered fibrillar structures, particularly, in the amorphous region of the P3HT. As shown in the AFM images (see, the phase images) in Figs. 4.4 (a) and 4.4(b), it was found that the fibrillar structures in the PX-P3HT layer were more pronounced than those in the DCB-P3HT layer. Furthermore, as shown in Fig. 4.4(c), the absorption peak at 601 nm (indicated by an arrow) suggests that the SA effect by the PX (being used as the solvent for the PCBM) strongly influences the structural order of the P3HT chains.

Based on the above results for the SA effect, I now describe the morphological changes of two PCBM-on-P3HT films, one of which was prepared on the PX-P3HT layer and the other on the DCB-P3HT layer. Figure 4.5 shows the AFM images and the UV-visible absorption spectra of the PCBM-on-P3HT films prepared by spin-coating the PCBM solution (1.5 wt.%) in the PX at the spinning rate of 1000 rpm onto two different P3HT

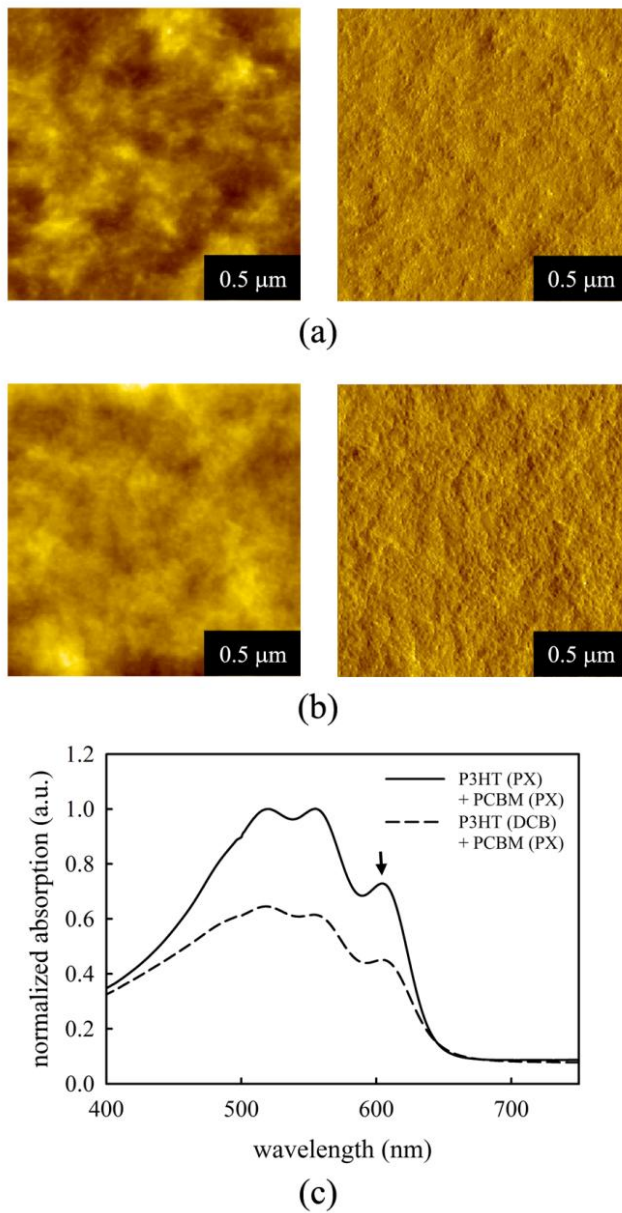


**Figure 4.5** The AFM images of the PCBM-on-P3HT films prepared from (a) the PX and (b) the DCB where the PCBM solution in the PX was spin-coated: The left and right columns are the amplitude and phase images, respectively. (c) The UV-visible absorption spectra of (a) and (b).

layers. As shown in Figs. 4.5(a) and 4.5(b), in both cases, the initial fibrillar morphology of the P3HT layer was substantially replicated in the PCBM-on-P3HT film after spin-coating the PCBM in the PX. For the case of the PCBM-on-P3HT from the PX, the ICFS was evidently evolved in the DBHJ configuration. However, for the DCB-P3HT case as shown in Fig. 4.5(c), the intensity of the absorption peak at about 601 nm was diminished in the PCBM-on-P3HT film compared to the P3HT layer itself. This tells us that during the preparation of the PCBM layer in the PX by spin-coating, the PX-P3HT layer prefers to produce the ICFS whereas the DCB-P3HT tends to form the IDS that were described in Fig. 4.1(b).

#### **4.1.4 Photovoltaic characteristics of P3HT/PCBM DBHJ**

The current-voltage curves of several DBHJ PV devices constructed using four different solvents (the PX, the CB, the DCB, and the CF) were shown in Fig. 4.6. The measurements were performed under illumination at the intensity of 100 mW/cm<sup>2</sup>. For the PX case, one PV device was treated with the post-annealing (PA) process at 150 °C for 3 min and the other no PA process. Note that as for organic thin-film-transistors [93], the PA treatment may also improve the electrical performance of organic solar cells [65, 78]. As shown in Fig. 4.6, for the CF and the CB cases, the PV characteristics were found to be quite poor due to the disruption of the P3HT layer during the subsequent PCBM process while for the PX case, the  $J_{sc}$  and the FF were

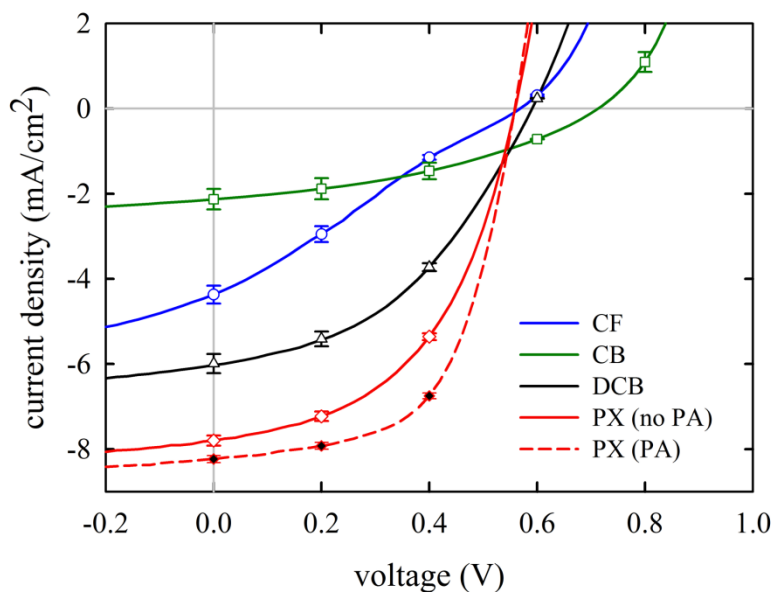


**Figure 4.6** Current-voltage characteristics of several DBHJ PV devices with the PCBM-on- P3HT films: the CF-P3HT (open circles), the CB-P3HT (open squares), the DCB-P3HT (open triangles), the PX-P3HT (open diamonds), and the PX-P3HT with the PA treatment (closed diamonds).

much enhanced because of the presence of the ICFS. Moreover, the PA treatment was found to further enhance the PV characteristics of the PX case. This is well consistent with what were observed in the AFM images and the UV-visible spectra of the PCBM-on-P3HT films as well as the P3HT layers as shown in Fig. 4.2 to Fig. 4.5. In fact, The IDS is barely transformed into the ICFS even under the PA, meaning that the enhancement of  $\eta_p$  by the PA is essentially limited. From the interfacial point of view, it is very interesting to note that the DCB case shows less fibrillar (or more amorphous) structures

than the PX case, and thus the formation of the subsequent PCBM layer on the P3HT layer will be different from each other. For the DCB case, the PCBM is expected to mix with the P3HT to form the IDS at a molecular level while for the PX case, it will be located separately from the fibrillar microcrystallites of the P3HT at a domain level as described in Fig. 4.1(b). As a consequence, the PX case showing the ICFS provides less interrupted pathways for charge transport and exhibits a lower value of the series resistance  $R_s = 7.34 \Omega\text{cm}^2$  and a higher FF (0.49) than the DCB case ( $R_s = 10.7 \Omega\text{cm}^2$  and FF = 0.43). A relatively small  $V_{oc}$  and a high FF were obtained for the PX case [94]. The performance parameters of the PV devices I studied, such as  $J_{sc}$ ,  $V_{oc}$ , FF, and  $\eta_p$ , were summarized in Table 4.1. As clearly seen in Table 4.1, due to the presence of the ICFS in the DBHJ, the PV device based on the PX-P3HT layer yields a relatively high value of  $\eta_p$  (at least 2%) among all the PV devices I constructed using four different solvents (the CF, the CB, the DCB, and the PX) without the PA treatment. The PX-P3HT device with the PA treatment shows the best PV performance of  $J_{sc} = 8.31 \text{ mA/cm}^2$ ,  $V_{oc} = 0.56 \text{ V}$ , FF = 0.59, and  $\eta_p = 2.73 \%$ . The increase of both  $J_{sc}$  and the FF results from the decrease in the series resistance (from  $7.34 \Omega\text{cm}^2$  to  $5.61 \Omega\text{cm}^2$ ) due to the PA process. This implies that the PA process contributes to the formation of percolated donor-acceptor networks for charge transport.

**Table 4.1** The values of  $J_{sc}$ ,  $V_{oc}$ , FF, and  $\eta_p$  in several DBHJ PV devices with the P3HT layers produced using four different solvents.

| PV Devices           | $J_{sc}$<br>(mA/cm <sup>2</sup> ) | $V_{oc}$<br>(V) | FF          | $\eta_p$<br>(%) |
|----------------------|-----------------------------------|-----------------|-------------|-----------------|
| CF-P3HT              | 4.37 ± 0.21                       | 0.57 ± 0.01     | 0.26 ± 0.02 | 0.63 ± 0.05     |
| CB-P3HT              | 2.13 ± 0.24                       | 0.71 ± 0.03     | 0.39 ± 0.02 | 0.59 ± 0.07     |
| DCB-P3HT             | 6.02 ± 0.16                       | 0.58 ± 0.01     | 0.42 ± 0.01 | 1.50 ± 0.06     |
| PX-P3HT              | 7.80 ± 0.12                       | 0.55 ± 0.01     | 0.49 ± 0.01 | 2.15 ± 0.03     |
| PX-P3HT<br>(with PA) | 8.23 ± 0.08                       | 0.56 ± 0.01     | 0.59 ± 0.01 | 2.70 ± 0.03     |

#### 4.1.5 Summary

I demonstrated that solvent-dependent fibrillar morphologies of the P3HT layer and the resultant PCBM-on-P3HT film play an important role in the PV characteristics of polymer-based DBHJ PV devices. Due to the solubility difference between the amorphous and crystalline, fibrillar structures in the P3HT layer, the PCBM prefers to diffuse into the amorphous region of the P3HT layer during the formation of the PCBM-on-P3HT film and consequently, the donor-acceptor interface becomes enlarged. The ICFS was found to be critical to induce high exciton generation/dissociation, to produce

spatially uninterrupted pathways for the charge transport, and to improve the power conversion efficiency of the PV device. It was found that both the surface roughness and the fibrillar morphology were varied with the solvent properties used for the solutions of both the P3HT and the PCBM, for example, whether good or poor, polar or non-polar, and high or low boiling temperature (vapor pressure). Among all the DBHJ PV devices I constructed using four different solvents (the CF, the CB, the DCB, and the PX), the PV device with the PX-P3HT layer showed the best PV characteristics of  $\eta_p \approx 2.7\%$  when it was post-annealed. The relatively low value of  $\eta_p$  compared to the previous results [72] may be enhanced by the purification of the active materials and the optimization of the solution concentration, the film thickness, and the device configuration. Our results showing the formation of the ICFS proposed in Fig. 4.1(b) will provide a versatile basis for understanding the physical mechanism associated with the PV phenomenon as well as for constructing a new class of the PV devices with high power conversion efficiency.

## **4.2 Integration of Polymer Solar Cells with MoO<sub>x</sub> Layer for Miniature High-voltage Source**

### **4.2.1 Introduction**

PSCs show great potential as a cost effective route to wide use of solar energy for electrical power generation [63-65, 95]. In the past decade, much effort has been made in enhancing the PCE of PSCs. However, the integration of PSCs is required for real power generation in solar cell module as well as the efficiency enhancement of single PSC. In addition, interest in high-voltage solar cells is motivated by application in microelectromechanical system (MEMS) and organic thin film transistors, which typically require operating voltages of tens of volts[96, 97]. Such solar cells provide a self-contained power supply that allows for autonomous MEMS and integrated organic electronic applications. To achieve high-voltage in a small area, the individual solar cells in the array need to be small, thus patterning techniques with high resolution are needed. Among the recently developed patterning techniques for fabricating highly integrated PSCs [98-100], photolithographically patterned electrodes used as a planar interconnection of nanomodels is presented [98]. However, this photolithographically patterned electrode method involves the patterning complexity and show the low fill factor of 25% and low PCE of 0.008%. An interesting variant approach is based on the use of patterned PEDOT:PSS by a mechanical scribing or the selective coating by

self assembling monolayer, which is rather simple but limits feature resolutions [99]. As another type, an advanced photolithographic methods, based on the use of an orthogonal solvent dissolving a new type of a photoresist, is promising for fabricating integrated organic devices but it inevitably experience the deterioration of underlying organic layers by the exposure of ultraviolet (UV) light and by the plasma etching [100].

For PSCs, hole transport layer (HTL) have important role due to the charge selective contacts between the photoactive layer (PL) and the anodes as shown in Fig. 4.7(a). In general, HTL of PEDOT:PSS is commonly utilized as a anode interfacial layer. PEDOT:PSS is, however, both hygroscopic and acidic with an associated reduction in device stability. Recently, molybdenum oxide ( $\text{MoO}_x$ ) as the anode interfacial layer is reported as an alternative of PEDOT:PSS, which improves the PCE and the increases the device stability because of its capability of better charge selective extracting and refractive index matching between the  $\text{MoO}_x$  and photoactive materials [46, 101, 102]. Basically, high open circuit voltage ( $V_{oc}$ ) is achieved by reducing the thermally generated dark current in single PSC device [103]. The  $V_{oc}$  is proportional to the logarithm of  $J_{ph}/J_s$ , suggesting that a small  $J_s$  result in a high  $V_{oc}$ , where  $J_{ph}$  is the photocurrent and  $J_s$  is the reverse dark saturation current.

In interconnected PSC array, new dark current paths are generated by interconnection of single PSC, which are dark current path through the PL and

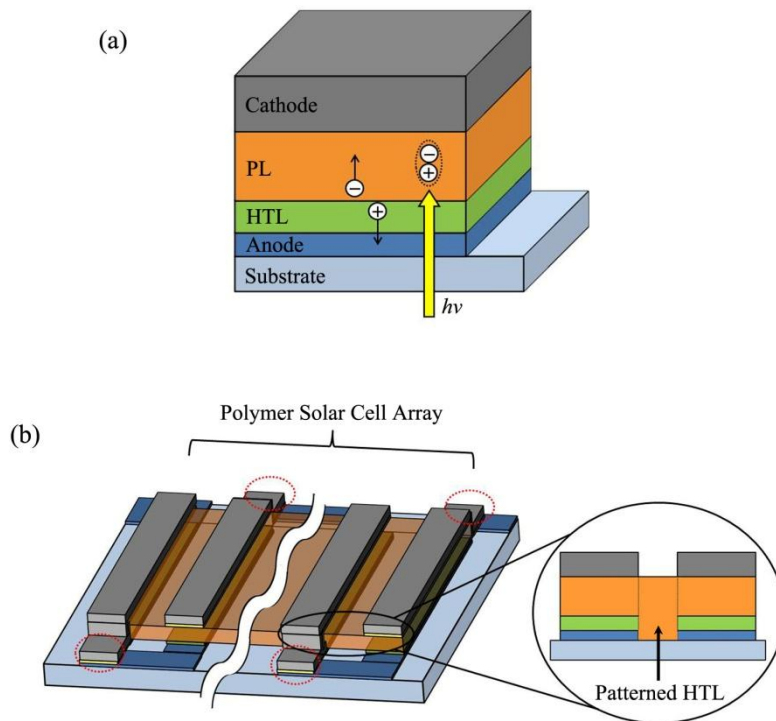


**Figure 4.7** The schematic illustration of (a) a PSC with hole transport layer (HTL) and (b) a PSC array structure with the patterned HTL.

path through the HTL. Moreover, the more each cell gap getting short through the high resolution patterning technique, the more dark current is generated. The exciton diffusion length is extremely short in conjugated polymer and conductivity of the PL are in the  $10^{-6} \sim 10^{-7}$  S/m range, which is six or seven orders of magnitude smaller than that of the  $\text{MoO}_x$  [63, 64, 104]. Therefore, patterning of the  $\text{MoO}_x$  with no deterioration is important to feature resolution and device performance. In this work, it is developed a powerful platform of

constructing polymer solar cells (PSCs) in a serial architecture within the framework of sacrificial layer-assisted patterning (SLAP) as shown in Fig. 4.7(b). The reduced dark current pathway by the SLAP of MoO<sub>x</sub> results in high open circuit voltage of integrated PSC array.

#### 4.2.2 Modeling the current path of integrated polymer solar cells with patterned HTL

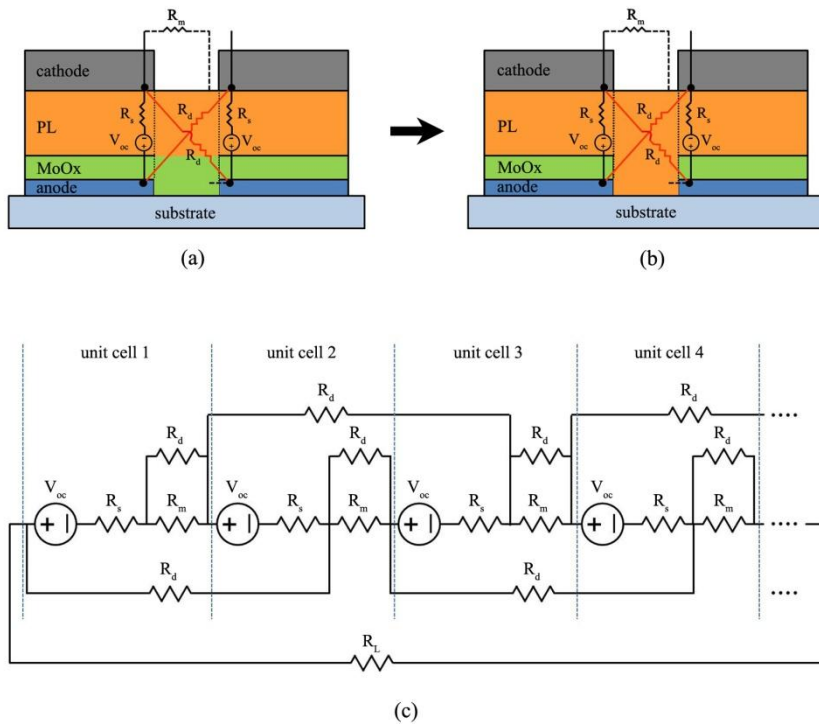


**Figure 4.8** The schematic illustration of (a) a PSC with hole transport layer (HTL) and (b) a PSC array structure with the patterned HTL.

As mentioned above, in interconnected PSC array, the new dark current paths are generated by interconnection of single PSC, which are dark current path through the PL and the HTL. I used MoO<sub>x</sub> as a HTL for selective hole extraction. Figure 4.8(a) and (b) show the interconnected PSC array with whole MoO<sub>x</sub> and patterned MoO<sub>x</sub>, respectively. The  $V_{oc}$ ,  $R_s$  and  $R_m$  represent voltage source, series resistance of unit cell, and interconnected resistance mainly derived from resistance of ITO. In this modeling, voltage source and series resistance substitute the unit PSC. For simplifying the single diode model of unit PSC, voltage source replace photo current source and contain parallel resistance and dark current in unit PSC. In ideal series connected PSC array, the resistance of dark current path of  $R_d$  are infinite. However, in this work,  $R_d$  are composed the sum of resistance of MoO<sub>x</sub> and PL. The calculated  $R_d$  for Fig. 4.8(a) and (b) cases are 8900  $\Omega/m$  and 17500  $\Omega/m$ , respectively. When  $V_{oc}$  of 0.5 V,  $R_s$  of 5  $\Omega/m$  and  $R_m$  of 1  $\Omega/m$  are inputted to the equivalent circuit of PSC array as shown in Fig. 4.8(c), the current density through the dark current path of  $J(R_d)$  correspond to Fig. 4.8(a) and (b) cases are  $0.93 \times 10^{-5}$  mA/cm<sup>2</sup> and  $0.48 \times 10^{-5}$  mA/cm<sup>2</sup>, respectively. From obtained values, it is expected that the high open circuit voltage is achieved in patterned MoO<sub>x</sub> PSC array by reduced dark current.

### 4.2.3 Fabrication process of integrated polymer solar cell using SLAP

Figure 4.9(a) shows the fabrication processes for the PSC arrays with patterned  $\text{MoO}_x$ . The corresponding microscopic images of the sacrificial layer (SL) patterns and the patterned  $\text{MoO}_x$  on ITO are shown in Fig. 4.9(b) and 4.9(c), respectively. Firstly, the ITO prepatterned glass substrate was cleaned sequentially with acetone, isopropyl alcohol, and methyl alcohol in an ultrasonicator for 10 min each. At each cleaning step, the substrate was rinsed with deionized water for 5 min in an ultrasonicator and purged with nitrogen gas. The cleaned substrates were dried at 90°C in a vacuum oven for 10 min to remove any residual water. For fabricating SL on ITO, a fluoruous polymer (3M Novec™ EGC-1700) was used as a SL which can be dissolved in a highly fluoruous solvent (3M Novec™ HFE-7100). Note that the fluoruous solvent is chemically inert to most of organic and inorganic materials, and is thus definitely able to be used in the process for PSCs [44, 105]. For the transfer printing to produce the SL patterns, a fluoruous polymer solution was coated on the surface of an elastomeric stamp of poly(dimethylsiloxane) (PDMS) having replica shapes of desired  $\text{MoO}_x$  patterns and then transfer-printed onto the ITO prepatterned substrate, shown in the Fig. 4.9(b). The SL patterns on PDMS stamp were easily transferred to the substrate without any additional treatment such as heat and/or pressure due to the low surface energy of the PDMS stamp compared to that of the glass substrate. Moreover,

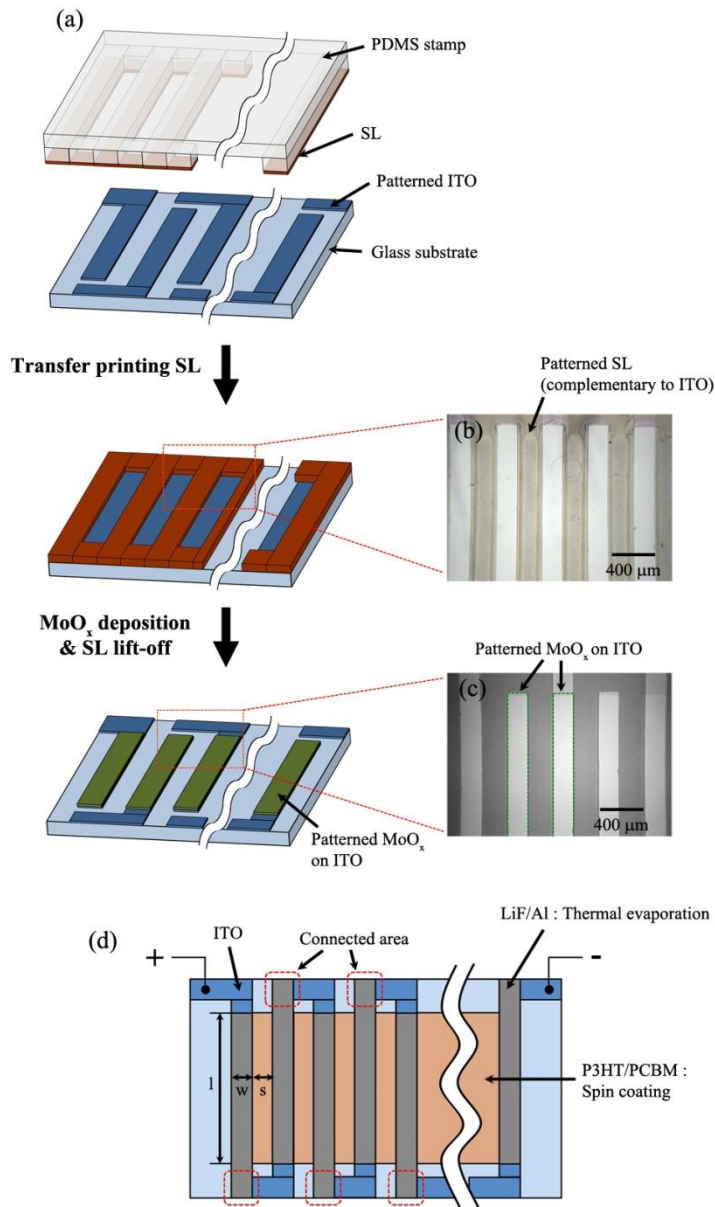


**Figure 4.9** (a) The fabrication process for SLAP and the corresponding microscopic image of top-view of (b) the patterned SL and (c) the patterned MoO<sub>x</sub>. The schematic diagram of the top-view of the fabricated PSC array with interconnected area.

the SL patterns down to a few micrometers can be achieved depending on the resolution of a PDMS stamp [44, 45, 106]. Then, after blanket-deposition of a MoO<sub>x</sub> layer (10 nm thick) over the substrate having SL patterns, the SL was lift-off in a fluorosolvent to leave out only the MoO<sub>x</sub> on ITO active regions, as shown in Fig. 4.9(c). The photoactive layer (PL) used in this study was prepared by dissolving 3 wt.% of the poly(3-hexylthiophene) (P3HT) and [6,6]-phenyl-C61-butyric acid methyl ester (PCBM) in chlorobenzene solution. The solution was spin-coated at 1000 rpm onto the MoO<sub>x</sub> deposited ITO glasses at room temperature. The thickness of the PL was determined to be about 140 nm. For the back metal electrode (cathode), a lithium fluoride (LiF) layer of 0.5 nm thick and an aluminum (Al) layer of 100 nm thick were successively prepared by thermal evaporation at the rate of 1 Å/s in a vacuum chamber. Figure 4.9 (d) shows the plan view of the complete device with each single cell length (l), width (w), and space (s). The final configuration is an array of 20 PSCs in series, with a length of 1.4 cm and the same value of widths and spaces is 500 μm. The fabricated cell was annealed at 150°C on a hotplate for 10 min. A total cell area was 1.4 cm<sup>2</sup> and I measured 10 cells for extracting average values. The photocurrent was measured under illumination from a solar simulator with AM 1.5G filters whose light intensity was calibrated with a standard silicon diode. The current-voltage characteristics were obtained using a source-measure unit (Model 2400, Keithley).

#### **4.2.4 Solar cell characteristics**

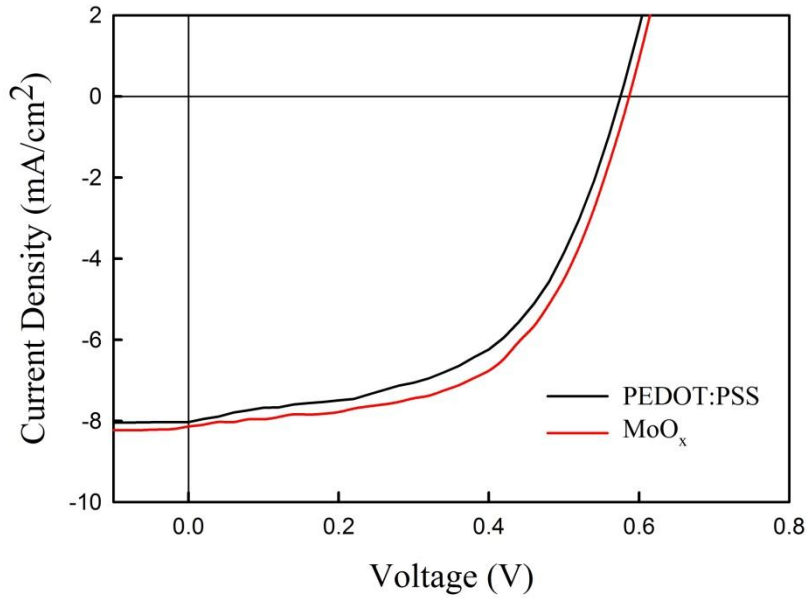


**Figure 4.10** Current-voltage characteristics of single PSC devices with the hole transport layer of PEDOT:PSS and MoO<sub>x</sub>.

The current-voltage curves of single PSC devices with PEDOT:PSS (red) and MoO<sub>x</sub> (black) under the AM 1.5 100mW/cm<sup>2</sup> illumination were shown in Fig. 4.10. As shown in Fig. 4. 10, PSC device with MoO<sub>x</sub> shows higher  $V_{oc}$  and PCE than that with PEDOT:PSS. This may be attributed to the deep highest occupied molecular orbital (HOMO) level of MoO<sub>x</sub> result in hole selective collecting from PL [46]. Therefore, PSC device with MoO<sub>x</sub> is appropriate HTL for the high voltage solar cell array.

The current-voltage curves of 20 PSC array with patterned (red) and whole (black) MoO<sub>x</sub> layer (a) under the AM 1.5 100mW/cm<sup>2</sup> illumination and (b) in the dark were shown in Fig. 4.11. The inset in Fig. 4.11(a) shows the

fabricated 20 PSC array with a total length of 2.0 cm and width of 2.4 cm. As shown in Fig. 4.11(a), for PSC array with whole MoO<sub>x</sub> layer cases, the V<sub>oc</sub> were found to be quiet poor due to the higher dark current than the PSC arrays with patterned MoO<sub>x</sub> layer. The relationship between dark current and V<sub>oc</sub> is inferred from [103, 107]

$$V_{oc} = \frac{nkT}{q} \ln\left(\frac{J_{ph}(V_{oc})}{J_s} + 1 - \frac{V_{oc}}{R_p J_s}\right), \quad (4.1)$$

where,  $n$  is the ideality factor,  $R_p$  is the parallel resistance. When  $J_{ph}/J_s \gg 1$ ,  $V_{oc}$  is proportional to  $\ln(J_{ph}/J_s)$  as mentioned above. The  $J_s$  of PSC arrays with patterned and whole MoO<sub>x</sub> are  $8.15 \times 10^{-6}$  mA/cm<sup>2</sup> and  $1.55 \times 10^{-5}$  mA/cm<sup>2</sup> as shown in Fig. 4.10(b). The logarithm factors of  $\ln(J_{ph}/J_s)$  in patterned and whole MoO<sub>x</sub> PSC arrays are 9.66 and 9.06, respectively. The V<sub>oc</sub> of above arrays are 10.11 V and 9.40 V, which is well matched with logarithm factors. The highest V<sub>oc</sub> of 10.11 volts and the fill factor (FF) of 0.49 were achieved from the 20 PSC array with patterned MoO<sub>x</sub> layer. The average voltage per cell of 0.505 volts and FF are similar or higher than the PSC array with patterned HTL and PL by mechanical scribing methods in similar number of PSC array [99]. These values are much higher than the PSC array with not patterned HTL and PL (voltage per cell of 0.43, FF of 0.13) [108]. It is noted that our PSC array with patterned MoO<sub>x</sub> layer show as good performance as PSC array with patterned HTL and PL and also have considerable potential for high resolution integration. The single PSCs with MoO<sub>x</sub>, shown in the Fig. 4.10, show the FF of 0.57. The FF difference between the single and array is due to

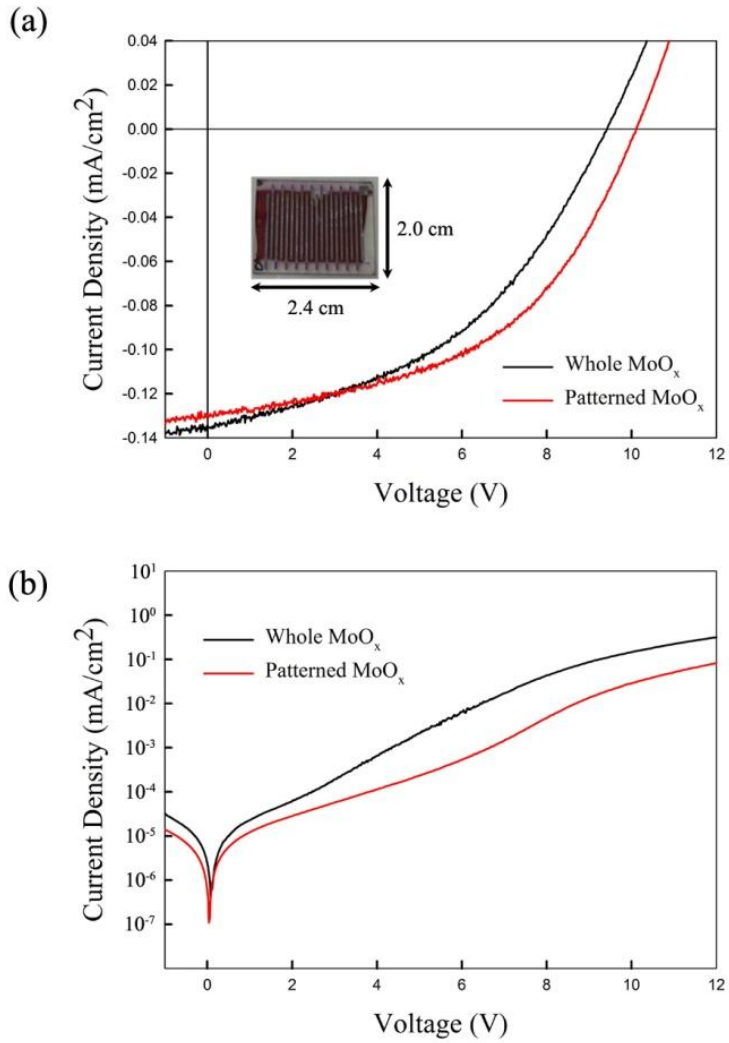


**Figure 4.11** The current-voltage curves of 20 PSC array with patterned (red) and whole (black) MoO<sub>x</sub> layer (a) under the AM 1.5 100mW/cm<sup>2</sup> illumination and (b) in the dark.

the 20 ITO-organic and organic-metal junctions, causing the increase of series resistance ( $R_s$ ) [100].

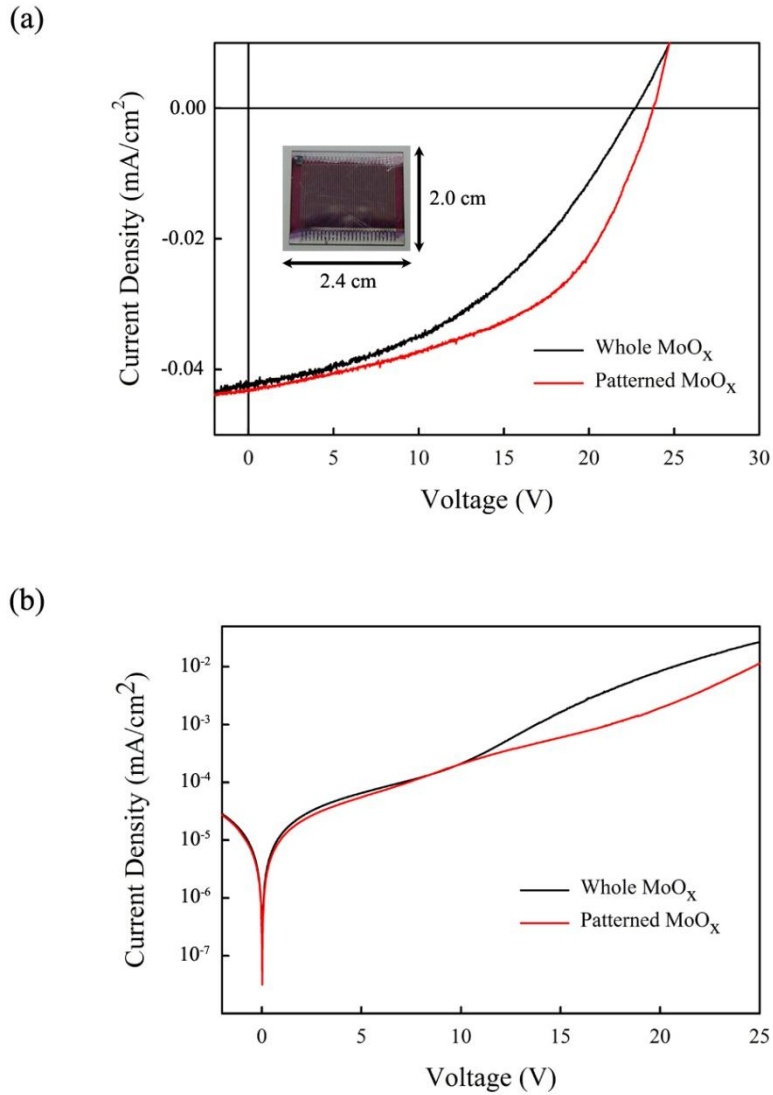


**Figure 4.12** The current-voltage curves of 50 PSC array with patterned (red) and whole (black) MoO<sub>x</sub> layer (a) under the AM 1.5 100mW/cm<sup>2</sup> illumination and (b) in the dark.

The current-voltage curves of 50 PSC array with patterned (red) and whole (black) MoO<sub>x</sub> layer (a) under the AM 1.5 100mW/cm<sup>2</sup> illumination and (b) in

the dark were shown in Fig. 4.12. The inset in Fig. 4.12(a) shows the fabricated 50 PSC array with a total length of 2.0 cm and width of 2.4 cm. As shown in Fig. 4.12(a), 50 PSC array with patterned MoO<sub>x</sub> layer shows higher  $V_{oc}$  than that with whole MoO<sub>x</sub> layer as like as 20 PSC array results. The  $J_{ph}$  of 50 PSC arrays with patterned and whole MoO<sub>x</sub> are  $4.3 \times 10^{-2}$  mA/cm<sup>2</sup> and  $4.2 \times 10^{-2}$  mA/cm<sup>2</sup>. The  $J_s$  of 50 PSC arrays with patterned and whole MoO<sub>x</sub> are  $1.97 \times 10^{-5}$  mA/cm<sup>2</sup> and  $2.75 \times 10^{-5}$  mA/cm<sup>2</sup> as shown in Fig. 4.12(b). The logarithm factors of  $\ln(J_{ph}/J_s)$  in patterned and whole MoO<sub>x</sub> PSC arrays are 7.69 and 7.33, respectively. The  $V_{oc}$  of above arrays are 23.77 V and 22.71 V, which is well matched with logarithm factors. The average voltage per cell of 0.475 volts is higher value in previous high integrated PSC array [98, 100]. It may be due to the hole selective collection of MoO<sub>x</sub>. The performance parameters of the single and array PSC devices, such as  $J_{sc}$ ,  $V_{oc}$ , FF, and PCE, were summarized in Table 4.2.

**Table 4.2** The values of  $J_{sc}$ ,  $V_{oc}$ , FF, and PCE in single and 20 PSC array devices with patterned  $MoO_x$  layer and whole  $MoO_x$  layer.

| PSC Devices                    | $J_{sc}$ (mA/cm <sup>2</sup> ) | $V_{oc}$ (V)     | FF              | PCE (%)         |
|--------------------------------|--------------------------------|------------------|-----------------|-----------------|
| Single (PEDOT:PSS)             | $8.01 \pm 0.25$                | $0.57 \pm 0.01$  | $0.54 \pm 0.02$ | $2.49 \pm 0.07$ |
| Single ( $MoO_x$ )             | $8.09 \pm 0.19$                | $0.59 \pm 0.01$  | $0.57 \pm 0.01$ | $2.72 \pm 0.06$ |
| 20 arrays (Whole $MoO_x$ )     | $0.134 \pm 0.016$              | $9.40 \pm 0.11$  | $0.44 \pm 0.03$ | $0.55 \pm 0.05$ |
| 20 arrays (Patterned $MoO_x$ ) | $0.129 \pm 0.017$              | $10.11 \pm 0.15$ | $0.49 \pm 0.03$ | $0.64 \pm 0.07$ |
| 50 arrays (Whole $MoO_x$ )     | $0.042 \pm 0.005$              | $22.71 \pm 1.13$ | $0.42 \pm 0.03$ | $0.40 \pm 0.04$ |
| 50 arrays (Patterned $MoO_x$ ) | $0.043 \pm 0.004$              | $23.77 \pm 1.05$ | $0.49 \pm 0.02$ | $0.51 \pm 0.04$ |

#### 4.2.5 Applicability for power source of electronic devices

To show an application of a PSC array as a new component in organic electronic systems, I present the operation of a liquid crystal display (LCD) by applying the high photovoltage of PSC array to the input voltage. As shown in Fig. 4.13(a), a prototype LCD of 6 cm wide and 4.5 cm long is well operated by a PSC array of 10 volts. The electro-optic transmittance of LCD used in this study appears at the threshold voltage of 2.5 V, and becomes to saturate

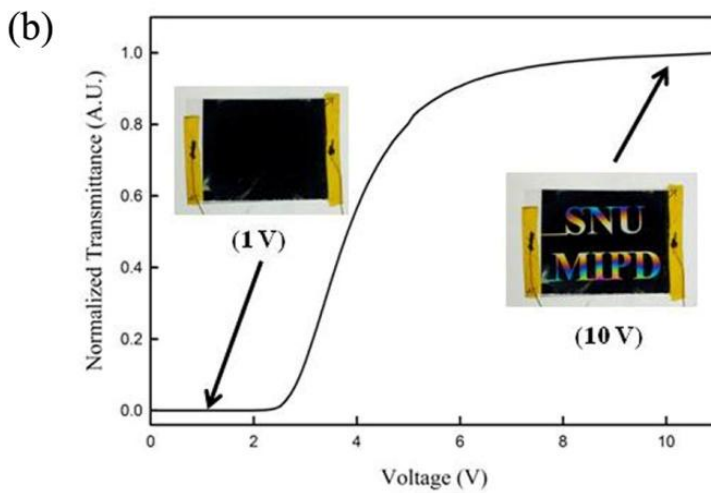
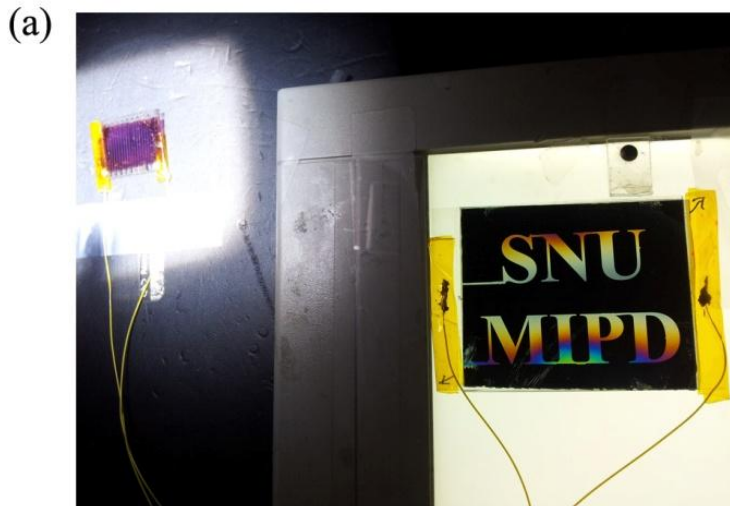


**Figure 4.13** The LCD device (a) operated by PSC array and (b) the normalized electro-optic transmittance as a function of the applied voltage.

above 7 V as shown in Fig. 4.13(b). This indicates that our PSC array is sufficiently applicable for the various electronic devices with proper voltages.

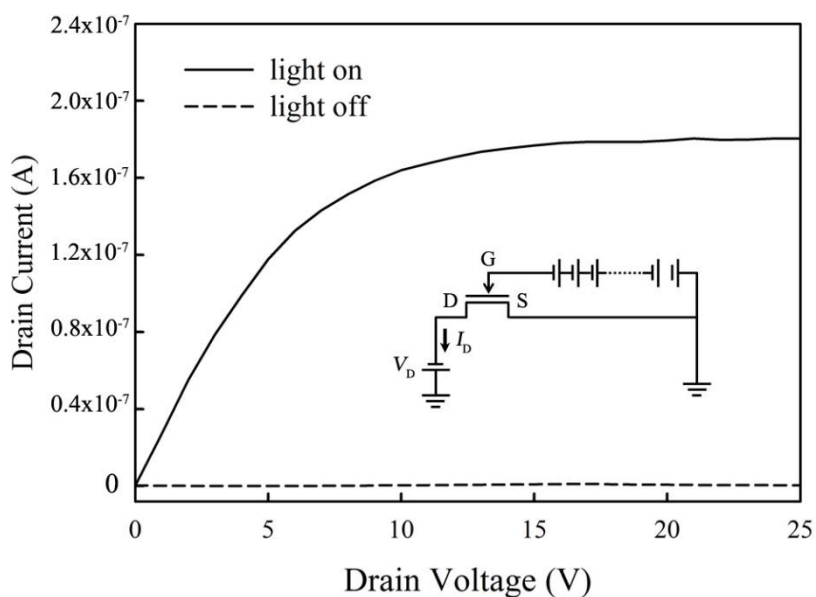


**Figure 4.14** Drain-source current-voltage characteristics of the OFET with gate bias voltage generated by the 50 PSC array under simulated solar irradiation and light off. The inset shows the electronic circuitry of the interconnected PSC array and the OFET.

As another application of a PSC array, we present the operation of an organic field-effect transistor (OFET) with a 50 PSC array providing the sufficiently high voltage. Figure 4.14 shows the output characteristic curves of the OFET with 50 PSC array and the circuitry is shown in the inset of Fig. 4.14. For preparation of OFET, a p-doped Si substrate and a layer of 300 nm-thick SiO<sub>2</sub> were used for the bottom gate electrode and an insulator, respectively. The leakage current of the OFET was about 0.1 nA at gate voltages between 0 and 40 V. The electrical characteristics of the 50 PSC

array connected with OFET were an open circuit voltages of 24 V and a short circuit current of 0.06 mA. The drain-source current-voltage ( $I_D$ - $V_D$ ) characteristics of the OFET were measured for a negative gate bias voltage generated by PSC array. As a result, the switching of the OFET by a 50 PSC array could be shown.

#### **4.2.6 Summary**

I developed a patterning technique based on SLAP to produce high resolution integrated PSC array for high voltage source of electronic devices. The SL patterns complementary to the active patterns can be generated by the transfer printing. By patterning HTLs, the lateral pathway of charges is block off, result in reducing the dark current and showing high output voltages. This generic patterning platform is expected to be applicable for constructing integrated PSCs in a cost-effective way.

## Chapter 5. Concluding Remarks

In this thesis, integrated solid-state dye-sensitized solar cells and polymer solar cells together with efficiency enhancement of single solar cell have been studied in the view point of patterning technique and performance improvement. I demonstrated highly integrated ss-DSC and PSC array show high open circuit voltage.

In Chap. 1, the principles and classification of solar cells were briefly introduced. Among various types of solar cells, next generation solar cell of DSC and PSC were described in detail. Also, the necessity of the development of a novel patterning approach optimized for organic materials was also emphasized as the motivation of this research on the development of high-fidelity patterning approach for organic solar cells.

In Chap. 2, the concept of using chemically stable/compatible sacrificial layer assisted patterning method for organic electronic devices. According to the combination of the method for patterning sacrificial layer and lift-off technique, high resolution patterning process for organic/inorganic materials was investigated. The material characteristics of the fluoros-polymer and fluoros-solvent were first described to guarantee the chemical compatibility for the use in the processing of organic materials and the patterning ability of transfer printing was demonstrated in the patterning of sacrificial layers. For practical application of such approach to the fabrication of OSC array, the

patterns of OSC device elements such as photo-anode of  $\text{TiO}_2$  in DSCs and hole transport material of  $\text{MoO}_x$  in PSCs were experimentally demonstrated.

The application of developed patterning approach to the fabrication of ss-DSC array was described in Chap. 3. By patterned  $\text{TiO}_2$  film of 2.5  $\mu\text{m}$  thick and use of solid state hole transport material, the fabrication of ss-DSC array were demonstrated. The fabricated ss-DSC array shows 6.68 V in 20 series interconnected cell.

In Chap. 4, in the view point of efficiency enhancement of single PSCs, the importance of solvent-dependent fibrillar morphologies of the P3HT layer and the resultant PCBM-on-P3HT film in the PV characteristics were described. Due to the solubility difference between the amorphous and crystalline, fibrillar structures in the P3HT layer, the PCBM prefers to diffuse into the amorphous region of the P3HT layer during the formation of the PCBM-on-P3HT film and consequently, the donor-acceptor interface becomes enlarged. The ICFS was found to be critical to induce high exciton generation/dissociation, to produce spatially uninterrupted pathways for the charge transport, and to improve the power conversion efficiency of the PV device. It was found that the fibrillar morphology were varied with the solvent properties used for the solutions of both the P3HT and the PCBM. Among all the DBHJ PV devices I constructed using four different solvents (the CF, the CB, the DCB, and the PX), the PV device with the PX-P3HT layer showed the best PV characteristics of  $\text{PCE} \approx 2.7\%$  when it was post-annealed. Our results showing the formation of the ICFS will provide a versatile basis for understanding the physical mechanism associated with the PV phenomenon as

well as for constructing a new class of the PV devices with high PCE. In addition, high resolution integrated PSC array for high voltage source were demonstrated. For fabricating PSC arrays in high resolution, sacrificial layer patterns complementary to the active patterns can be generated by the transfer printing. By patterning HTLs, the lateral pathway of charges is block off, result in PSC arrays showing reduced dark current and high output voltages.

In conclusion, throughout this thesis, integrated polymer and dye-sensitized solar cell for high voltage sources have been explored. Novel patterning method to produce the high resolution integration for organic-based devices have been proposed and demonstrated. Researches on the integrated organic solar cells are highly expected to provide a foundation for realizing the potentials of practical applications.

## Bibliography

- [1] “Annual Energy Outlook 2010” U.S Energy Information Administration (EIA) (<http://www.eia.gov>).
- [2] M. I. Hoffert, K. Caldeira, A. K. Jain, E. F. Haites, L. D. D. Harvey, S. D. Potter, M. E. Schlesinger, S. H. Schneider, R. G. Watts, T. M. L. Wigley, and D. J. Wuebbles, *Nature* **395**, 881, (1998).
- [3] H. Khatib, *Energy Policy* **48**, 737, (2012).
- [4] M. Yu, Y. -Z. Long, B. Sun, and Z. Fan, *Nanoscale* **4**, 2783, (2012).
- [5] Sharp, *Photovoltaic Roadmap 2030*, the New Energy and Industrial Technology Development Organization.
- [6] J. Nelson, *The Physics of Solar Cells*, Imperial College Press, London (2003).
- [7] T. L. Benanti and D. Venkataraman, *Photosynth. Res.* **87**, 73 (2006).
- [8] M. A. Green, K. Emery, Y. Hishikawa, W. Warta, and E. D. Dunlop, *Prog. Photovolt: Res. Appl.* **20**, 606 (2012).
- [9] Research Cell Efficiency Plot for Various Photovoltaic Technologies 1976–2012 (<http://www.nrel.gov>)
- [10] J. C. Bernede, *J. Chil. Chem. Soc.* **53**, 1549 (2008).
- [11] M. A. Green. *Third Generation Photovoltaics: Advanced Solar Energy Conversion*. Springer-Verlag , Berlin Heidelberg (2003).
- [12] H. Spanggaard, F. C. Krebs, *Sol. Energy Mater. Sol. Cells*, **83**, 125 (2004).

- [13] C. J. Brabec, N. S. Sariciftci, and J. C. Hummelen, *Adv. Funct. Mater.* **11**, 15 (2001).
- [14] M. Gratzel, *J. Photochem. Photobiol. C - Photo.* **4**, 145 (2003).
- [15] C. W. Tang, *Appl. Phys. Lett.* **48**, 183 (1986).
- [16] N. S. Sariciftci, L. Smilowitz, A. J. Heeger, and F. Wudl, *Science*, **258**, 1474 (1992).
- [17] B. A. Gregg and M. C. Hanna, *J. Appl. Phys.* **93**, 3605 (2003).
- [18] S. R. Forrest, *MRS bull.* **30**, 28 (2005).
- [19] P. Peumans, A. Yakimov, and S. R. Forrest, *J. Appl. Phys.* **93**, 3693 (2003).
- [20] B. O'Regan and M. Gratzel, *Nature*, **353**, 737 (1991).
- [21] A. Mishra, M. K. R. Fischer, and P. Bauerle, *Angew. Chem. Int. Ed.* **48**, 2474 (2009).
- [22] N. Robertson, *Angew. Chem. Int. Ed.* **45**, 2338 (2006).
- [23] S. Y. Huang, G. Schlichthorl, A. J. Nozik, M. Gratzel, and A. J. Frank, *J. Phys. Chem. B.* **101**, 2576 (1997).
- [24] J. Bisquert, F. Fabregat-Santiago, I. Mora-Sero, G. Garcia-Belmonte, and S. Gilmanez, *J. Phys. Chem. C* **113**, 17278 (2009).
- [25] P. Wang, S. M. Zakeeruddin, J. E. Moser, M. K. Nazeeruddin, T. Sekiguchi, and M. Gratzel, *Nat. Mater.* **2**, 402 (2003).
- [26] U. Bach, D. Lupo, P. Comte, J. E. Moser, F. Weissortel, J. Salbeck, H. Spreitzer, and M. Gratzel, *Nature*, **395**, 583 (1998).
- [27] B. Li, L. Wang, B. Kang, P. Wang, and Y. Qiu, *Sol. Energy Mater. Sol. Cells*, **90**, 549 (2006).

- [28] C. S. Karthikeyan and M. Thelakkat, *Inorg. Chim. Acta*, **361**, 635 (2008).
- [29] M. M. Ling and Z. Bao, *Chem. Mater.*, **16**, 4824 (2007).
- [30] C. N. Hoth, S. A. Choulis, P. Schilinsky, and C. J. Brabec, *Adv. Mater.*, **19**, 3973 (2007).
- [31] H. Sirringhaus, T. Kawase, R. H. Friend, T. Shimoda, M. Inbasekaran, W. Wu, E. P. Woo, *Science*, **290**, 2133 (2000).
- [32] H. Sirringhaus, T. Kawase, R. H. Friend, *Mater. Res. Bull.*, **26**, 539 (2001).
- [33] J. Bharathan and Y. Yang, *Appl. Phys. Lett.*, **72**, 2660 (1998).
- [34] A. A. Zakhidov, J. -K. Lee, H. H. Fong, J. A. DeFranco, M. Chatzichristidi, P. G. Taylor, C. K. Ober, and G. G. Malliaras, *Adv. Mater.*, **20**, 3481 (2008).
- [35] H. S. Hwang, A. A. Zakhidov, J. -K. Lee, X. Andre, J. A. DeFranco, H. H. Fong, A. B. Holmes, G. G. Malliaras, and C. K. Ober, *J. Mater. Chem.*, **18**, 3087 (2008).
- [36] S. -I. Na, S. -S. Kim, J. Jo, S. -H. Oh, J. Kim, and D. -Y. Kim, *Adv. Funct. Mater.*, **18**, 3956 (2008).
- [37] I. -K. Ding, J. Zhu, W. Cai, S. -J. Moon, N. Cai, P. Wang, S. M. Zakeeruddin, M. Gratzel, M. L. Brongersma, Y. Cui, and M. D. McGehee, *Adv. Energy Mater.*, **1**, 52 (2011).
- [38] M. D. Austin and S. Y. Chou, *Appl. Phys. Lett.*, **81**, 4431 (2002).
- [39] J. A. Rogers, Z. Bao, and L. Dhar, *Appl. Phys. Lett.*, **73**, 294 (1998).
- [40] E. Menard, M. A. Meitl, Y. Sun, J. -U. Park, D. J. Shir, Y. -S. Nam, S. Jeon, and J. A. Rogers, *Chem. Rev.*, **107**, 1117 (2007).

- [41] H. Tavana and A.W. Neumann, *Advances in Colloid and Interface Science*, **132**, 1 (2007).
- [42] S.Wu, *Polymer Interface and Adhesion*, Marcel Dekker, Boca Raton, pp 96-104 (1982).
- [43] Z. Wang, J. Zhang, R. Xing, J. Yuan, D. Yan, and Y Han, *J. Am. Chem. Soc.*, **125**, 15278 (2003).
- [44] W. Choi, M. -H. Kim, Y. -J. Na, and S. -D. Lee, *Org. Electron.*, **11**, 2026 (2010).
- [45] W. Choi, M. -H. Kim, and S. -D. Lee, *Jpn. J. Appl. Phys.*, **50**, 080219 (2011).
- [46] Y. Sun, C. J. Takacs, S. R. Cowan, J. H. Seo, X. Gong, A. Roy, and A. J. Heeger, *Adv. Mater.*, **23**, 2226 (2011).
- [47] D. Y. Kim, J. Subbiah, G. Sarasqueta, F. So, H. Ding, Irfan, and Y. Gao, *Appl. Phys. Lett.*, **95**, 093304 (2009).
- [48] M. Gratzel, *Inorg. Chim.*, **44**, 6841 (2005).
- [49] Y. Chiba, A. Islam, Y. Watanabe, R. Komiya, N. Koide, and L. Han, *Jpn. J. Appl. Phys., Part 2*, **45**, L638 (2006).
- [50] F. Gao, Y. Wang, D. Shi, J. Zhang, M. Wang, X. Jing, R. Humphry-Baker, P. Wang, S. M. Zakeeruddin, and M. Gratzel, *J. Am. Chem. Soc.*, **130**, 10720 (2008).
- [51] H. J. Snaith, and L. Schmidt-Mende, *Adv. Mater.*, **19**, 3187 (2007).
- [52] I. -K. Ding, N. Tetreault, J. Brilllet, B. E. Hardin, E. H. Smith, S. J. Rosenthal, F. Sauvage, M. Gratzel, and M. D. McGehee, *Adv. Funct. Mater.*, **19**, 2431 (2009).

- [53] J. Melas-Kyriazi, I. -K. Ding, A. Marchioro, A. Punzi, B. E. Hardin, G. F. Burkhard, N. Tetreault, M. Gratzel, J. -E. Moser, and M. D. McGehee, *Adv. Energy Mater.*, **1**, 407 (2011).
- [54] L. Yang, U. B. Cappel, E. L. Unger, M. Karlsson, K. M. Karlsson, E. Gabrielsson, L. Sun, G. Boschloo, A. Hagfeldt, and M. J. Johansson, *Phys. Chem. Chem. Phys.*, **14**, 779 (2012).
- [55] J. K. Koh, J. Kim, B. Kim, J. H. Kim, and E. Kim, *Adv. Mater.*, **23**, 1641 (2011).
- [56] S. Norasetthekul, P. Y. Park, K. H. Baik, K. P. Lee, J. H. Shin, B. S. Jeong, V. Shishodia, E. S. Lambers, D. P. Norton, and S. J. Pearton, *Appl. Surf. Sci.*, **185**, 27 (2001).
- [57] G. Dang, H. Cho, K. P. Ip, S. J. Pearton, S. N. G. Chu, J. Lopata, W. S. Hobson, L. M. F. Chirovsky, and F. Ren, *J. Electrochem. Soc.*, **148**, G25 (2001).
- [58] J. Kim, J. K. Koh, B. Kim, J. H. Kim, and E. Kim, *Angew. Chem. Int. Ed.*, **51**, 6864 (2012).
- [59] Z. Zhang, S. M. Zakeeruddin, B. C. O`Regan, R. Humphry-Baker, and M. Gratzel, *J. Phys. Chem. B*, **109**, 21818 (2005).
- [60] Chemical structure provided by Solaronix SA  
(<http://www.solaronix.com>)
- [61] C. S. Karthikeyan, H. Wietasch, and M. Thelakkat, *Adv. Mater.*, **19**, 1091 (2007).
- [62] C. Zhang, J. Zhang, Y. Hao, Z. Lin, and C. Zhu, *J. Appl. Phys.*, **110**, 064504 (2011).

- [63] C. J. Brabec, *Sol. Energy Mater. Sol. Cells*, **83**, 273 (2004).
- [64] S. Gunes, H. Neugebauer, and N. S. Sariciftci, *Chem. Rev.*, **107**, 1324 (2007).
- [65] G. Li, V. Shrotriya, J. Huang, Y. Yao, T. Moriarty, K. Emery, and Y. Yang, *Nat. Mater.*, **4**, 864 (2005).
- [66] D. Lee, W. K. Bae, I. Park, D. Y. Yoon, S. Lee, and C. Lee *Sol. Energy Mater. Sol. Cells*, **95**, 365 (2011).
- [67] L. Chen, D. Godovsky, O. Inganäs, J. C. Hummelen, R. A. J. Janssens, M. Svensson, and M. R. Andersson, *Adv. Mater.*, **12**, 1367 (2000).
- [68] M. M. Alam and S. A. Jenekhe, *Chem. Mater.*, **16**, 4647 (2004).
- [69] T. Kietzke, H. H. Hörhold, and D. Neher, *Chem. Mater.*, **17**, 6532 (2007).
- [70] S. V. Chasteen, J. O. Härter, G. Rumbles, J. C. Scott, Y. Nakazawa, M. Jones, H. H. Hörhold, H. Tillman, and S. A. Carter, *J. Appl. Phys.*, **99**, 033709 (2006).
- [71] L. Xue, L. Liu, Q. Gao, S. Wen, J. He, and W. Tian, *Sol. Energy Mater. Sol. Cells*, **93**, 501 (2009).
- [72] K. H. Lee, P. E. Schwenn, A. R. G. Smith, H. Cavaye, P. E. Shaw, M. James, K. B. Krueger, I. R. Gentle, P. Meredith and P. L. Burn, *Adv. Mater.*, **23**, 766 (2011).
- [73] D. Chen, F. Liu, C. Wang, A. Nakahara, and T. P. Russell, *Nano Lett.*, **11**, 2071 (2011).
- [74] M. Granstrom, K. Petrits, A. C. Arias, A. Lux, M. R. Andersson, and R. H. Friend, *Nature*, **395**, 257 (1998).

- [75] M. Drees, K. Premaratne, W. Graupner, J. R. Helflin, R. M. Davis, D. Marciu, and M. Miller, *Appl. Phys. Lett.*, **81**, 4607 (2002).
- [76] M. Drees, R. M. Davis, and J. R. Helflin, *J. Appl. Phys.*, **97**, 036103 (2005).
- [77] K. Kim, J. Liu, and D. L. Carroll, *Appl. Phys. Lett.*, **88**, 181911 (2006).
- [78] X. Jiang, J. Dai, J. Wang, and D. Yan, *Thin Solid Films*, **516**, 6487 (2008).
- [79] M. Kaur, A. Gopal, R. M. Davis, and J. R. Helflin, *Sol. Energy Mater. Sol. Cells*, **93**, 1779 (2009).
- [80] R. J. Kline, M. D. McGehee, E. N. Kadnikova, J. Liu, J. M. J. Frechet, and M. F. Toney, *Macromolecules*, **38**, 3312 (2005).
- [81] J. Liu, M. Arif, J. Zou, S. I. Khondaker, and L. Zhai, *Macromolecules*, **42**, 9390 (2009).
- [82] S. Berson, R. D. Bettingnies, S. Bailly, and S. Guillerez, *Adv. Func. Mater.*, **17**, 1377 (2007).
- [83] K. J. Ihn, J. Moulton, and P. Smith, *J. Polym. Sci. Part B: Polym. Phys.*, **31**, 735 (1993).
- [84] X Yang, J. Loss, S. C. Veenstra, W. J. H. Verhees, M. M. Wienk, J. M. Kroon, M. A. J. Michels, and R. A. J. Janssen, *Nano Lett.*, **5**, 579 (2005).
- [85] S. Bertho, W. D. Oosterbann, V. Vrindts, J. D'Haen, T. J. Cleij, L. Lutsen, and D. Vanderzande, *Org. Electron.*, **10**, 1248 (2009).
- [86] L. Li, G. Lu, and X. Yang, *J. Mater. Chem.*, **18**, 1984 (2008).
- [87] J. S. Kim, J. H. Lee, J. H. Park, C. Shim, M. Sim, and K. Cho, *Adv. Funct. Mater.*, **21**, 480 (2011).

- [88] M. J. Winokur, and W. Chunwachirasiri, *Journal of Polymer Science: Part B: Polymer Physics*, **41**, 2630 (2003).
- [89] S. C. B. Mannsfeld, M. L. Tang, and Z. Bao, *Adv. Mater.*, **23**, 127 (2011).
- [90] P. J. Brown, D. S. Thomas, A. Kohler, J. S. Wilson, J. S. Kim, C. M. Ramsdale, H. Sirringhaus, and R. H. Friend, *Phys. Rev. B*, **67**, 064203 (2003).
- [91] G. Bidan, S. Guillerez, and V. Sorokin, *Adv. Mater.*, **8**, 157 (1996).
- [92] T. Yamamoto, D. Komarudin, M. Arai, B. L. Lee, H. Suganuma, N. Asakawa, Y. Inoue, K. Kubota, S. Sasaki, T. Fukuda, and H. Matsuda, *J. Am. Chem. Soc.*, **120**, 2047 (1998).
- [93] J. -H. Bae, J. Park, C. -M. Keum, W. -H. Kim, M. -H. Kim, S. O. Kim, S. K. Kwon, and S. -D. Lee, *Org. Electron.*, **11**, 784 (2010).
- [94] V. Shrotriya, J. Ouyang, R. J. Tseng, G. Li, and Y. Yang, *Chem. Phys. Lett.*, **411**, 138 (2005).
- [95] H. S. Chen, J. Hou, S. Zhang, Y. Liang, G. Yang, Y. Yang, L. Yu, Y. Wu, G. Li, *Nat. Photon.*, **3** 649 (2009).
- [96] J. B. Lee, Z. Chen, M. G. Allen, A. Rohatgi, and R. Arya, *J. Microelectromechanical Syst.*, **4**, 102 (1995).
- [97] T. Sakakibara, H. Izua, T. Shibata, H. Tarui, S. Kenichi, S. Kiyama, and N. Kawahara, *Sensors and Actuators A*, **95**, 208 (2002).
- [98] M. Niggemann, W. Graf, and A. Gombert, *Adv. Mater.*, **20**, 4055 (2008).
- [99] M. Niggemann, B. Zimmermann, J. Haschke, M. Glatthaar, and A. Gombert, *Thin Solid Films*, **516**, 7181 (2008).
- [100] Y. F. Lim, J. K. Lee, A. A. Zakhidov, J. A. DeFranco, H. H. Fong, P. G. Taylor, C. K. Ober, and G. G. Malliaras, *J. Mater. Chem.*, **19**, 5394 (2009).

- [101] C. Tao, S. Ruan, X. Zhang, G. Xie, L. Shen, X. Kong, W. Dong, C. Liu, and W. Chen, *Appl. Phys. Lett.*, **93**, 193307 (2008).
- [102] J. Subbiah, P. M. Beaujuge, K. R. Choudhury, S. Ellinger, J. R. Reynolds, and F. So, *Org. Electron.*, **11**, 955 (2010).
- [103] N. Li, B. E. Lassiter, R. R. Lunt, G. Wei, and S. R. Forrest, *Appl. Phys. Lett.*, **94**, 023307 (2009).
- [104] E. A. I. Saad, *J. Optoelectron. Adv. Mater.*, **7**, 2743 (2005).
- [105] J. Obrzut, and K. A. Page, *Phys. Rev. B*, **80**, 195211 (2009).
- [106] C. M. Keum, J. H. Bae, M. H. Kim, and S. -D. Lee, *Org. Electron.*, **13**, 778 (2012).
- [107] B. P. Rand, D. P. Bulk, and S. R. Forrest, *Phys. Rev. B*, **75**, 115327 (2007).
- [108] J. Lewis, J. Zhang, and X. Jiang, *J. Renewable and sustainable energy*, **1**, 013101 (2009).

## Publication

### [1] International Journals

1. **S.-M. Cho**, M.-H. Kim, C. M. Keum, S.-D. Lee, “Integrated polymer solar cells with charge transporting  $\text{MoO}_x$  layer through sacrificial layer-assisted patterning”, (*in preparation*).
2. **S.-M. Cho**, M.-H. Kim, S. -U. Kim, S.-D. Lee, “Micropatterning of  $\text{TiO}_2$  photo-electrode for integration of solid state dye-sensitized solar cells on a single substrate”, (*in preparation*).
3. **S.-M. Cho**, J.-H. Bae, E. Jang, M.-H. Kim, C. Lee, S.-D. Lee, “Solvent effect of the fibrillar morphology on the conversion efficiency of a polymer photovoltaic cell in a diffusive heterojunction”, *Semicond. Sci. Technol.* **27**, 125018 (2012).
4. J.-H. Na, **S.-M. Cho**, S.-D. Lee, and Y.-W. Lim, “High brightness and wide-view transflective liquid crystal display with two in-cell imprinted optical films in an inverse-twisted-nematic geometry”, *J. Inf. Disp* **12**, 11 (2011).
5. S. Hwang, J. Min, M.-G. Lee, K. Choe, H.-Y. Choi, Y.-T. Kim, **S.-M Cho**, and S.-D. Lee, “Novel wide viewing liquid crystal display with improved off-axis image quality in a twisted nematic configuration”, *Opt. Engin.* **48**, 114001 (2009).

6. **S.-M Cho**, J.-H. Hong, Y.-T. Kim, and S.-D. Lee, “Adhesive-transfer bonding technique for flexible liquid crystal displays with high mechanical stability”, *Mol. Cryst. Liq. Cryst.* **513**, 1 (2009).
7. J.-H. Hong, **S.-M Cho**, Y.-T. Kim, and S.-D. Lee, “Formation of surface microstructure arrays by selective wettability for wide-viewing liquid crystal displays”, *Mol. Cryst. Liq. Cryst.* **507**, 161 (2009).
8. Y.-T. Kim, J.-H. Hong, **S.-M Cho**, and S.-D. Lee, “Viewing angle switchable liquid crystal display with double layers separated by an interlayer support”, *Jpn. J. Appl. Lett.* **48**, 110205 (2009).
9. Y.-T. Kim, J.-H. Hong, **S.-M Cho**, and S.-D. Lee, “Fabrication of a dual gap substrate using the replica-molding technique for transfective liquid crystal displays”, *J. Inf. Disp.* **10**, 68 (2009).
10. J.-H. Hong, **S.-M Cho**, Y.-T. Kim, and S.-D. Lee, “Etchingless fabrication of bi-level microstructures for liquid crystal displays on plastic substrates”, *J. Inf. Disp.* **9**, 6 (2008).

## [2] International Conferences

1. **S.-M. Cho**, S. -U. Kim, M. -H. Kim, and S.-D. Lee, “High-voltage power source based on integration of dye-sensitized solar cells using the lift-off process of sacrificial layer” MRS Spring Meeting (San Francisco, USA, 2012) W4.28
2. (Invited) Y.-W. Lim, **S.-M. Cho**, J.-H. Na, and S.-D. Lee, “Wide-viewing transflective liquid crystal display with in-cell binary optical layer in an inverse twisted nematic geometry”, Adv. Disp. Mater. & Devi. (Daegu, Korea, 2010).
3. **S.-M. Cho**, C.-M. Keum, E. Jang, and S.-D. Lee, “Importance of the fibrillar morphology for the device performances of a polymer photovoltaic device with a diffusive heterojunction structure”, The 6th International Conference on Organic Electronics (Paris, France, 2010) p. 118.
4. C.-M. Keum, J. -H. Bae, **S.-M. Cho**, and S.-D. Lee, “Deposition rate dependence of the initial layer growth of pentacene on a topologically modified polymeric insulator”, The 6th International Conference on Organic Electronics (Paris, France, 2010) p. 71.
5. **S.-M. Cho**, Y.-W. Lim, J.-H. Hong, S. -C. Park and S.-D. Lee, “Transflective liquid crystal display having an in-cell wire grid polarizer in a twisted nematic geometry”, Int’l Sym. Liq. Cryst. Sci. Tech. (Kunming, China, 2009) ID064.
6. J.-H. Hong, **S.-M. Cho**, Y.-T. Kim, and S.-D. Lee, “Direct formation

of bi-level microstructures for wide-viewing liquid crystal displays with plastic substrates”, Proc. 8<sup>th</sup> Int’l Meeting Inf. Disp. (Korea Inf. Disp. Soc., Seoul, 2008) p. 1286.

7. E. Jang, J.-H. Hong, **S.-M. Cho**, and S.-D. Lee, “A polymer heterojunction photovoltaic device with a diffusive region by selective interpenetration”, Int’l Sym. Mol. Mater. Chem. (Toulouse, France, 2008) ID095.
8. (Invited) **S.-M. Cho**, J.-H. Hong, Y.-T. Kim, and S.-D. Lee, “Polymer-based bonding techniques for improving mechanical stability of flexible liquid crystal displays”, Adv. Disp. Mater. & Devi. (Jeju, Korea, 2008) p. 31.
9. Y.-T. Kim, S. Hwang, **S.-M. Cho**, and S.-D. Lee, “Viewing-angle switchable liquid crystal display in a tandem configuration”, 22<sup>nd</sup> Int’l Liq. Cryst. Conf. (Jeju, Korea, 2008) p. 274.

## 국문 초록

화석 연료를 대체할 수 있는 신 재생 에너지에 대한 관심이 증가함에 따라, 태양빛을 전기로 변환할 수 있는 태양전지가 각광을 받고 있다. 특히 저가 공정이 가능한 유기 태양전지, 즉 고분자 태양전지나 염료 감응형 태양전지에 대한 연구가 전세계적으로 활발히 진행되고 있다. 지난 십 수년간 유기 태양전지 관련 연구는 실리콘 기반의 태양전지보다 상대적으로 낮은 효율 향상에 집중되어 있었다. 하지만 유기 태양전지를 통해 실제 전력을 생산하고 유기 태양전지를 전자 소자의 전원으로 활용하기 위해서는 효율 향상뿐 만 아니라 집적 기술을 발전이 함께 이루어져야 한다. 이러한 관점에서, 유기 태양전지 분야에서 집적화 연구가 이루어졌으나 아직은 매우 초기 단계로, 낮은 신뢰성과 화학적 부적합성, 낮은 해상도 등으로 인해 실제 유기 전자 소자 제작에는 이용되지 못하고 있다. 그리하여 유기 태양전지 집적화에 적합한 고신뢰 및 고해상도 패턴 기술의 개발이 필요하다.

본 논문에서는 유기물에 성능 저하를 일으키기 않는 화학적 적합성을 갖는 불소계 고분자 희생층을 기반으로 상보적 전사 후 리프트-오프 기술을 적용하여 유기 태양전지의 집적화를 이루고 이를 실제 전자 소자에 응용하는 방안을 탐색한다. 소프트

리소그래피의 트랜스퍼 공정을 사용하여 불소계 고분자를 원하는 패턴과 상보적으로 패턴한 후 패턴하고자 하는 소자의 박막을 입히고 불소계 고분자를 리프트-오프하면 간단하게 패턴을 형성할 수 있다. 이러한 패턴 기술은 유기 박막의 특성을 저하시키지 않으며 수 마이크로미터 수준의 고해상도 패턴 제작이 가능하다. 또한 유/무기 박막을 따로 또는 동시에 패턴 가능한 장점이 있다.

이러한 패턴 제작 기술을 바탕으로, 염료 태양전지를 집적하여 어레이를 제작하는 방법을 개발하였다. 기존의 염료 태양전지는 17 나노미터 정도 크기의  $\text{TiO}_2$  나노 입자로 이루어진 광 전극층을 패턴하는 방법이 존재하지 않아 고집적 어레이 관련 연구가 이루어지지 못했다. 본 연구에서는 희생층 패터닝 공정을 사용하여 광 전극층을 이루는 나노 입자를 마이크로 스케일로 패턴하고 액체 전해질을 고체 전해질로 대체함으로써 염료 감응형 태양전지 어레이를 제작하였다. 고체 전해질을 사용할 경우 액체를 가두는 각각의 격벽이 필요하지 않아 손쉽게 고해상도의 염료 감응형 태양전지 어레이를 제작할 수 있다.

다음으로, 유기 태양전지 중 고분자 태양전지의 단위 소자 효율 향상과 집적화에 대해 소개한다. 먼저, 고분자 태양전지의 고효율화에서는 고분자 태양전지의 이중 층 구조에서 공액 고분자의 용매 변화에 따른 파이브릴라 구조 형성과 효율과의 상관 관계를 밝혔다. 공액 고분자인 P3HT 의 용매로 용해도가 낮은

용매를 사용하였을 때에 파이프릴라 구조가 나타나며 이를 이중 층 구조로 제작하기 위해 공액 고분자 위에 PCBM 을 코팅하면 결정성이 높은 파이프릴라 영역과 결정성이 낮은 부분의 용해도 차이에 의해 결정성이 낮은 부분으로만 PCBM 이 파고들어 P3HT 와 PCBM 의 계면이 넓어지고 전하의 이동 통로가 잘 형성되어 효율이 향상된다. 용해도가 낮은 *p*-xylene 용매를 사용하였을 때 2.7%, 용해도가 높은 chlorobenzene 용매를 사용하였을 때 0.5%의 소자 효율이 나타났다. 또한 비등점이 높은 용매일 수록 파이프릴라 구조 형성에 좋은 영향을 미치는 것을 밝힘으로써 앞으로의 유기 태양전지 효율 향상에 있어 용매의 선택의 중요함을 밝히고 앞으로의 초석을 세웠다.

마지막으로, 희생층 패터닝 공정을 사용하여 고집적의 고성능 고분자 태양전지 어레이를 제작하고 이를 직렬 연결하여 유기 전자 소자의 고전압 구동 전원으로 적용하였다. 기존에 정공 수송층으로 사용되던 PEDOT:PSS 대신 정공만 선택적으로 받아들여 성능이 좋은 MoO<sub>x</sub> 를 정공 수송층으로 사용하고 이를 패터닝 하여 고전압 고분자 태양전지 어레이 제작이 가능하였다. 그리고 제작된 소자를 액정 디스플레이와 전계 효과 트랜지스터의 구동 전원으로 활용하여 고전압 고분자 태양전지 어레이의 활용성을 보이고 새로운 응용분야를 모색하였다.

결론적으로, 본 논문에서는 유기 태양전지 단위 소자의 효율 향상과 단위 소자를 집적한 태양전지 어레이 제작에 대하여 탐색하였다. 단위 소자의 효율 향상에 있어 고분자 물질에 적합한 유기 용매의 선택이 중요함을 보였으며, 패터닝 기술을 사용하여 단위 소자를 좁은 면적에 집적함으로써 고전압 태양전지 어레이를 제작하고 이를 액정 디스플레이 및 유기 박막 트랜지스터 동작 전원으로 적용하였다. 본 연구에서 제안한 유기 태양전지의 효율 향상 및 집적화 기술은 저비용 고효율 유기 태양전지 소자의 다양한 응용분야를 창출하는데 기술적 초석을 제공할 것으로 기대된다.

주요어: 유기 태양전지, 고분자 태양전지, 염료 감응형 태양전지, 태양전지 어레이, 패터닝 기술, 전사-인쇄

학번: 2008-30886